Oxidative steam reforming of ethanol over Ir/CeO2 catalysts: A structure sensitivity analysis

Weijie Cai, Fagen Wang, C. Daniel, Andre C van Veen, Y. Schuurman, C. Descorme, H. Provendier, Wenjie Shen, Claude Mirodatos

Oxidative steam reforming of ethanol over Ir/CeO_2 catalysts: A structure sensitivity analysis

Weijie Cai [a], Fagen Wang [b], Cécile Daniel [a], Andre C. van Veen [a,c], Yves Schuurman [a], Claude Descorme [a], Hélène Provendier [a], Wenjie Shen [b,*], Claude Mirodatos [a,*]

[a] *University of Lyon – Institut de recherches sur la catalyse et l'environnement de Lyon (IRCELYON, UMR 5256, CNRS – Université Claude Bernard Lyon 1), 69626 Villeurbanne Cedex, France*
[b] *State Key Laboratory of Catalysis, Dalian Institute of Chemical Physics, Chinese Academy of Sciences, Dalian 116023, China*
[c] *Ruhr University Bochum, Laboratory of Industrial Chemistry, 44780 Bochum, Germany*

A series of Ir/CeO_2 catalysts of different oxide and metallic phase dispersions was investigated by XRD, TPR, HRTEM, CO_2 TPD/calorimetry, *in situ* DRIFT spectroscopy, and oxygen isotopic exchange techniques in order to elucidate the specific influence of catalyst morphology and structure on the oxidative steam reforming (OSR) of ethanol. Structure/texture sensitivity is demonstrated on the basis of the OSR mech-anism, which involves, in order: (i) ethanol adsorption on the ceria surface, (ii) partial oxidation to acetate and surface migration of the C2 intermediates along the ceria support toward the Ir particles, (iii) crack-ing and further oxidation into Ir carbonyls and ceria carbonates, and (iv) hydrogen and carbon monoxide desorption from the Ir particles. Structure sensitivity is established by considering two types of sites: the ceria surface sites, which are essentially pairs of oxygen vacancies and basic OH groups, as well as interfacial sites between Ir and ceria phases, involving pairs of Ir coordinately unsaturated sites (CUSs) and the aforementioned peripheral ceria sites. This structure sensitivity is revealed by TOF calculations based on these two types of sites, which correspond to the two main rate controlling steps of the ethanol OSR mechanism, namely steps (ii) and (iii). The materials considered display activity, selectivity, and resistance to aging (manifested by coke deposition and sintering) that are closely related to their initial structure and texture. Two domains in terms of iridium and ceria particle size are identified, leading either to stable and selective catalysts or to unstable and unselective catalysts. Such an original and quantified structure sensitivity analysis should prove useful for further process development.

1. Introduction

Hydrogen, a clean energy carrier, presents the potential to generate electricity in a highly efficient manner through the use of fuel cell technology. While the direct distribution and storage of hydrogen are the principal drawbacks to domestic or remote area uses, on-site generation from various H-containing feedstocks deserves to be investigated. Hydrogen production by oxidative steam reforming of bio-ethanol is therefore a valuable strategic target due to: (i) its ease of feedstock transport compared to conventional natural gas steam reforming, (ii) the renewable character of bio-ethanol compared to fossil fuels, and (iii) its increasing industrial production, which now makes it available for various domestic uses [1,2].

Metals such as Ni, Cu, Rh, and Pt [3,4] have been found to exhibit reasonable intrinsic activity for the oxidative steam reforming of ethanol. Furthermore, numerous oxides such as CeO_2, Al_2O_3, MgO, and ZrO_2 have been investigated as a support for the metal phase in order to ensure optimal metallic dispersion and stability but also to participate directly in the catalytic process [5–7]. It has frequently been shown that both the active metal and the support play a critical role in the activity and stability of the catalyst for hydrocarbon or oxygenate reforming [8,9]. In this respect, the excellent performance of CeO_2-supported catalysts, which present high catalytic activity and resistance against carbon deposition, has been tentatively related to the high oxygen storage capacity (OSC) of ceria [10,11] and to the strong interaction between ceria and the supported metal [12,13]. For example, Kugai et al. [14,15] found that Ni–Rh catalysts supported on high surface area CeO_2 nanocrystals showed better performance for the oxidative steam reforming of ethanol than did catalysts with a lower specific surface area. They stressed that significant differences in catalytic properties (such as metallic dispersion) and in performance (such as activity and selectivity) could be linked to the differences in CeO_2 supports. An explanation for these effects remains to be established; however, while the structural and textural

* Corresponding authors.
E-mail address: claude.mirodatos@ircelyon.univ-lyon1.fr (C. Mirodatos).

morphology of the catalyst (metallic dispersion and specific surface area of the ceria support) deserves more thorough investigation and control in view of industrial application.

Our group has previously described the outstanding performance of a well-dispersed Ir/CeO_2 catalyst for the oxidative steam reforming of ethanol [16,17]. Upon long-term testing, moderate ceria sintering was observed but had negligible impact on the iridium dispersion. Nevertheless, the full conversion of ethanol in the aforementioned experiments prevented the precise investigation of the potential effect of the specific surface area of the ceria support on catalyst performance and aging. We consequently performed an in-depth study of the combined effect of the ceria surface area and the iridium dispersion on the performance of the Ir/CeO_2 catalyst for the oxidative steam reforming of ethanol. For this purpose, catalysts with different ceria grain sizes but with the same Ir loading, including the catalyst already described in [16,17], were compared under identical reaction conditions. In order to further analyze the performance of the catalysts, their intrinsic properties were characterized using Temperature-Programmed Reduction (TPR), X-Ray Diffraction (XRD), oxygen storage capacity (OSC), oxygen isotopic exchange (SSITKA), *in situ* DRIFT spectroscopy, and High-Resolution Transmission Electron Microscopy (HRTEM) imaging, with an aim to establish possible structure–activity relationships.

2. Experimental

2.1. Catalyst preparation

CeO_2 was prepared by precipitation, with diammonium cerium (IV) nitrate made to react with urea in aqueous solution, according to the procedure detailed in [17]. After filtration and thorough washing with water, the excess water was evaporated under vacuum, the precipitate was dried at 100 °C for 12 h, and finally calcined at 400, 550, 700, or 850 °C for 5 h in static air, yielding ceria samples with different specific surface areas (labeled as Ce400, Ce550, Ce700, and Ce850, respectively).

The series of Ir/CeO_2 catalysts loaded with 2 wt.% Ir was prepared by deposition–precipitation according to the procedure reported in [17]. The catalysts prepared were named Ir/Ce400, Ir/Ce550, Ir/Ce700, and Ir/Ce850. Their Ir content is reported in Table 1. Less than 0.03 wt.% sodium was detected by chemical analysis, which rules out any significant role of alkali for these catalysts.

2.2. Catalyst characterization

2.2.1. XRD

XRD patterns were recorded using a Rigaku D/MAX-RB diffractometer equipped with a Cu Kα radiation source operating at 40 kV and 100 mA. The mean crystallite sizes of ceria were calculated according to the Debye–Scherrer equation.

2.2.2. HRTEM

HRTEM images were obtained using a Philips Tecnai G^220 microscope operating at 300 kV. The samples were prepared by ultrasonically suspending the sample in ethanol. A droplet of the suspension was deposited onto a thin carbon film supported on a standard copper grid and then dried in air.

2.2.3. BET

N_2 adsorption–desorption isotherms were recorded at −196 °C using a Nova 4200e instrument (Quantachrome). Prior to measurements, the sample was outgassed at 300 °C for 2 h under primary-pump vacuum. The specific surface area was calculated by multi-point BET analysis of the nitrogen adsorption isotherms.

2.2.4. H_2 chemisorption

The dispersion of the metallic phase obtained after reduction in hydrogen was calculated from H_2 chemisorption. Experiments were performed at low temperature to limit the "spillover" phenomenon [18,19] using a pulse chromatographic apparatus. After reduction under flowing hydrogen at 400 °C for 1 h, the sample was cooled to room temperature under flowing argon. The reactor was then placed in a dry ice–acetone mixture at −85 °C, and pulses of hydrogen were injected until saturation was indicated by constant peak area of the final pulses. This permitted the evaluation of total hydrogen uptake (H_{C1}). Subsequently, the catalyst was flushed for 10 min under argon to remove the physically adsorbed hydrogen molecules, and hydrogen was pulsed again until saturation (H_{C2}). The amount of chemisorbed hydrogen was calculated using $H_C = H_{C1} - H_{C2}$.

2.2.5. H_2-TPR

Hydrogen temperature-programmed reduction (H_2-TPR) was performed with a conventional setup equipped with a TCD detector. A 100 mg catalyst sample (40–60 mesh) was pretreated at 300 °C for 1 h under flowing He (40 mL/min). After cooling to room temperature, the sample was exposed to a flow of 5 vol.% H_2/He (40 mL/min), and the temperature was increased linearly at 10 °C/min.

2.2.6. OSC

The oxygen storage capacity (OSC) was measured in a microreactor coupled with a quadrupole mass spectrometer (Omnistar, Balzers). Before analysis, the sample (100 mg) was reduced with 5 vol.% H_2/Ar (50 mL/min) at 650 °C. The sample was purged for 15 min at 650 °C using flowing Ar. A stream of 5 vol.% O_2/Ar (50 mL/min) was then passed through the sample, and the oxygen consumption was quantitatively monitored with the mass spectrometer at $m/e = 32$.

2.2.7. Carbon deposition

The carbon deposition occurring during catalytic testing was investigated by temperature-programmed oxidation (TPO)

Table 1
Physicochemical properties and oxygen storage capacity of the fresh catalysts and in parenthesis, values measured after long-term aging treatments carried out at 650 °C for 60 h.

Catalyst	x_{Ir} [a] (wt.%)	D_{Ir} [b] (%)	S_{BET} [c] (m^2/g_{cat})	d_{CeO2} [d] (nm)	$S_{external}$ [e] (m^2/g_{cat})
Ir/Ce400	1.92	67 (61)	153 (61)	6 (15)	140 (56)
Ir/Ce550	1.81	62 (46)	102 (43)	8 (19)	105 (44)
Ir/Ce700	1.87	59 (37)	45 (20)	15 (34)	56 (25)
Ir/Ce850	1.75	26 (23)	16 (12)	44 (60)	19 (14)

[a] Ir content from chemical analyses (no significant changes have been noted after long-run testing).
[b] Ir dispersion calculated from hydrogen chemisorption after reduction at 400 °C under flowing H_2 for the fresh samples and from HRTEM images for the used samples (see Fig. 14).
[c] BET surface area measured by N_2 adsorption before and after long-term runs.
[d] Ceria grain size, calculated from the XRD patterns (Debye–Scherrer equation).
[e] Ceria surface calculated from the ceria grain size using the formula $S_{external} = \frac{60{,}000}{\rho_{ceria}\ (g\ cm^3) \times d\ (Å)}$.

conducted in a continuous-flow fixed-bed quartz reactor equipped with an online mass spectrometer (IPC400, INFICON). Here, 50 mg of the used catalyst was loaded, and using a feed flow of 5 vol.% O_2/Ar (100 mL/min), the system was heated from room temperature to 800 °C at a constant rate of 5 °C/min. The effluent composition was quantitatively measured by mass spectrometry.

2.2.8. SSITKA

The oxygen exchange dynamics for the various catalysts was determined by $^{16}O_2/^{18}O_2$ steady-state isotopic transient kinetic analysis (SSITKA), with abrupt switches from a flow of $^{16}O_2$ to the same flow of $^{18}O_2$. The $^{16}O_2/^{18}O_2$ exchange was monitored by maintaining an unchanged overall oxygen concentration (steady-state conditions) [20–22]. A catalyst sample of 50 mg was loaded in a tubular quartz reactor and outgassed under Ar at 400 °C for 15 min. The reactor was then heated to 650 °C to perform the $^{16}O_2/^{18}O_2$ exchange experiments. The signals at m/z = 32 ($^{16}O_2$), 34 ($^{16}O^{18}O$), 36 ($^{18}O_2$), 28 (N_2, to monitor possible air leaks), 40 (Ar), and 4 (He) were continuously monitored by online mass spectrometry (IPC400, INFICON) during the exchange process. A tracer gas (5 vol.% He) was added to the 2 vol.% O_2/Ar flow (total flow: 200 mL/min) to quantify the gas-phase holdup [23,24]. Blank experiments showed that no exchange occurred in the absence of catalyst.

2.2.9. CO_2-TPD

In order to evaluate the basicity of the oxide surface, CO_2-TPD experiments were carried out in a quartz reactor. Prior to the TPD runs, the catalyst (125 mg) was initially reduced under flowing 8 vol.% H_2/Ar (25 mL/min) for 2 h at 400 °C and then cooled down to 30 °C under flowing Ar. The adsorption of CO_2 was carried out using a feed mixture of 4 vol.% CO_2/Ar for 20 min. The reactor was then purged with Ar for 10 min. The temperature was increased to 600 °C with a heating rate of 10 °C/min under Ar flow. A mass spectrometer (IPC400, INFICON) was used for online monitoring of the effluent gases.

2.2.10. Calorimetry

The basicity of the oxide surface was also evaluated by adsorption of CO_2, followed by microcalorimetry. The adsorption enthalpy of CO_2 was measured by differential scanning calorimetry (DSC) using a Sensys evo DSC instrument (Setaram) equipped with a 3D thermal flow sensor. The sample was loaded into twin fixed-bed reactors, with one reactor serving as a reference. The sample was reduced in a mixture of 8 vol.% H_2 in Ar for 2 h at 400 °C and then cooled down to 30 °C under Ar flow. A flowing mixture of 10% CO_2/N_2 was then admitted to the catalyst at 30 °C, until the adsorption sites were saturated, *i.e.*, when CO_2 was detected at the outlet of the calorimeter reactor by online mass spectrometry. The exothermic peak corresponding to CO_2 adsorption was integrated to provide the total enthalpy of adsorption for the amount of CO_2 adsorbed. The mean heat of adsorption per mole of adsorbed CO_2 was determined by considering the total amount of CO_2 adsorbed until its reappearance at the calorimeter outlet (breakthrough curve). This amount was verified using CO_2 TPD experiments performed under similar conditions (adsorption at saturation followed by TPD) using a greater amount of catalyst for higher accuracy.

2.2.11. In situ DRIFT

In situ DRIFT spectra were recorded using a Nicolet 8700 spectrometer equipped with a DTGS-Tec detector as well as a Harrick scientific cell designed for high-temperature use and fitted with a ZnSe window designed for *in situ* measurements. Spectra were collected at a resolution of 4 cm^{-1}, with an average of 32 scans. A sample of about 40 mg, sieved to yield a particle fraction around 100 μm in size, was loaded onto a layer of silicon carbide particles to improve the thermal exchange. The sample was first reduced under a 50 mL/min flow of a 4:1 Ar/H_2 mixture, for 4 h at 400 °C. The catalyst was cooled down to 30 °C under flowing Ar (50 mL/min). Ethanol adsorption was carried out at 30 °C by admitting a 50 mL/min flow of Ar bubbling through a saturator filled with ethanol held at 0 °C. The spectra were recorded continuously to monitor surface saturation. When the DRIFT spectra were stabilized, a purge under Ar was applied for 30 min before the TPD was started at 5 K/min under Ar.

2.3. Catalytic measurements under steady-state conditions

The oxidative steam reforming of ethanol was conducted in a continuous-flow fixed-bed quartz reactor at atmospheric pressure. For this, 300 mg of catalyst (250–400 μm) was loaded and maintained between two layers of quartz wool. Before the reaction, the catalyst was reduced under 5 vol.% H_2/He (30 mL/min) at 400 °C for 1 h. The feed stream was composed of ethanol/water/O_2 (1:1.8:0.6 molar ratio) without a diluting gas, according to the stoichiometric equation already shown to be effective for OSR in [17]:

$$CH_3CH_2OH + 1.8H_2O + 0.6O_2 \rightarrow 4.8H_2 + 2CO_2$$

Pure ethanol (0.023 mL/min, liquid) and water (0.013 mL/min, liquid) were fed by an HPLC pump to a vaporizer heated to 200 °C; the vapors were mixed with an oxygen stream (5.3 mL/min) dosed by a mass-flow controller. The GHSV for the reaction was 6000 mL g_{cat}^{-1} h^{-1}, unless otherwise specified. The effluent from the reactor was analyzed online using gas chromatography. H_2, CO, and CO_2 were separated in a packed column (HayeSep D) and analyzed using a thermal conductivity detector (TCD) with He as the carrier gas. Hydrocarbons and oxygenates were separated with a capillary column (INNOWAX) and analyzed with a flame ionization detector (FID).

The ethanol conversion was calculated according to:

$$X_{EtOH} = \left\{[\Sigma n^*(C_i)_{outlet}] - \left[2^*(C_{EtOH})_{outlet}\right]\right\} / \left[\Sigma n^*(C_i)_{outlet}\right] \quad (1)$$

with $(C_i)_{outlet}$: molar concentration of carbon-containing species (labeled as i) in the outlet gas (n = 1 for CO, CO_2, and CH_4; n = 2 for C_2H_6, C_2H_4, CH_3CH_2OH, and CH_3CHO; n = 3 for CH_3COCH_3).

The molar concentration of hydrogen in the dry outlet gas (except water) was calculated according to:

$$C^*_{H2} = (C_{H2})_{outlet} / \left[(C_{H2})_{outlet} + \Sigma(C_i)_{outlet}\right] \quad (2)$$

with $(C_{H2})_{outlet}$/molar concentration of hydrogen in the dry outlet gas.

The molar concentrations of carbon-containing species (labeled as i) in the dry outlet gas were calculated according to:

$$C^*_i = (C_i)_{outlet} / \left[(C_{H2})_{outlet} + \Sigma(C_i)_{outlet}\right] \quad (3)$$

3. Results

3.1. Characterization of fresh catalysts

3.1.1. Structural and textural measurements (BET, XRD, and HRTEM)

Table 1 reports the specific surface areas established by the BET method for the fresh catalysts, along with the crystallite sizes of the support determined by XRD. The specific surface area decreased by one order of magnitude from 153 m^2/g for Ir/Ce400 down to 16 m^2/g for Ir/Ce850. All CeO_2 samples show only the XRD patterns for a fluorite-type oxide structure [16,17]. With increasing calcination temperatures, the CeO_2 XRD patterns become sharper, indicating an increasing particle size as reported

in Table 1 (d_{CeO2}). Table 1 also reports the surface area calculated from the ceria mean grain diameter derived from XRD measurements ($S_{external}$). Since these values are quite close to the ones determined by N_2 adsorption, it can be concluded that the ceria grains are essentially monocrystalline, which rules out any significant concentration of bulk crystal defects.

As also shown in Table 1, the metallic dispersion (D_{Ir}) obtained after reduction (1 h at 400 °C under H_2 flow) was around 60% for Ir/Ce400, Ir/Ce550, and Ir/Ce700, but only 26% for the Ir/Ce850 catalyst. The process of Ir oxide reduction to metallic particles at 400 °C was therefore only slightly dependent on the ceria surface area within the 153–45 m^2/g_{cat} range, but led to a much less dispersed metallic phase on the strongly sintered ceria (16 m^2/g_{cat}) of the sample calcined at 850 °C. Later, this feature will be discussed in terms of the SMSI effect related to the surface concentration of the ceria defects.

In line with the findings from XRD, HRTEM images (Fig. 1) clearly show a significant increase in the ceria particle size with increasing calcination temperature. As for the iridium phase, no small Ir (metal or oxide) particles were observed on the calcined Ir/Ce400, Ir/Ce550, and Ir/Ce700 samples, due to the poor contrast with the CeO_2 support phase. After a severe calcination pretreatment (Ir/Ce850), some IrO_2 particles (~3 nm) were observed at the edge of sintered ceria particles (Fig. 1L), corresponding to an iridium dispersion of about 30%, which is close to the dispersion determined from hydrogen adsorption on the reduced sample (26%) (Table 1).

3.1.2. Surface characterization (in situ DRIFT)

To investigate the state of the ceria surface before adsorption and catalysis, DRIFT spectra were recorded over a 25–500 °C temperature range under flowing Ar (50 mL/min) after an initial heat treatment under dry air. Fig. 2 presents the IR spectra of the hydroxyl domain recorded at 100 °C, where the spectra are well-differentiated between the tested samples. As can be seen, superimposed with a broad band typical of weakly adsorbed water, OH groups ranging from strongly basic to less basic entities (3730, 3670, 3650–3620 cm^{-1}) are detected on the Ir/Ce400 and Ir/Ce550 samples and, to a lesser extent, on Ir/Ce700. By contrast, the bands have practically vanished for the Ir/Ce850 sample. The OH groups observed on the high surface area Ir/Ce400 sample are still observed at 600 °C, though they are not as well resolved, while the surface carbonates, corresponding to the typical bands at 1200–1700 cm^{-1}, are progressively decomposed as confirmed

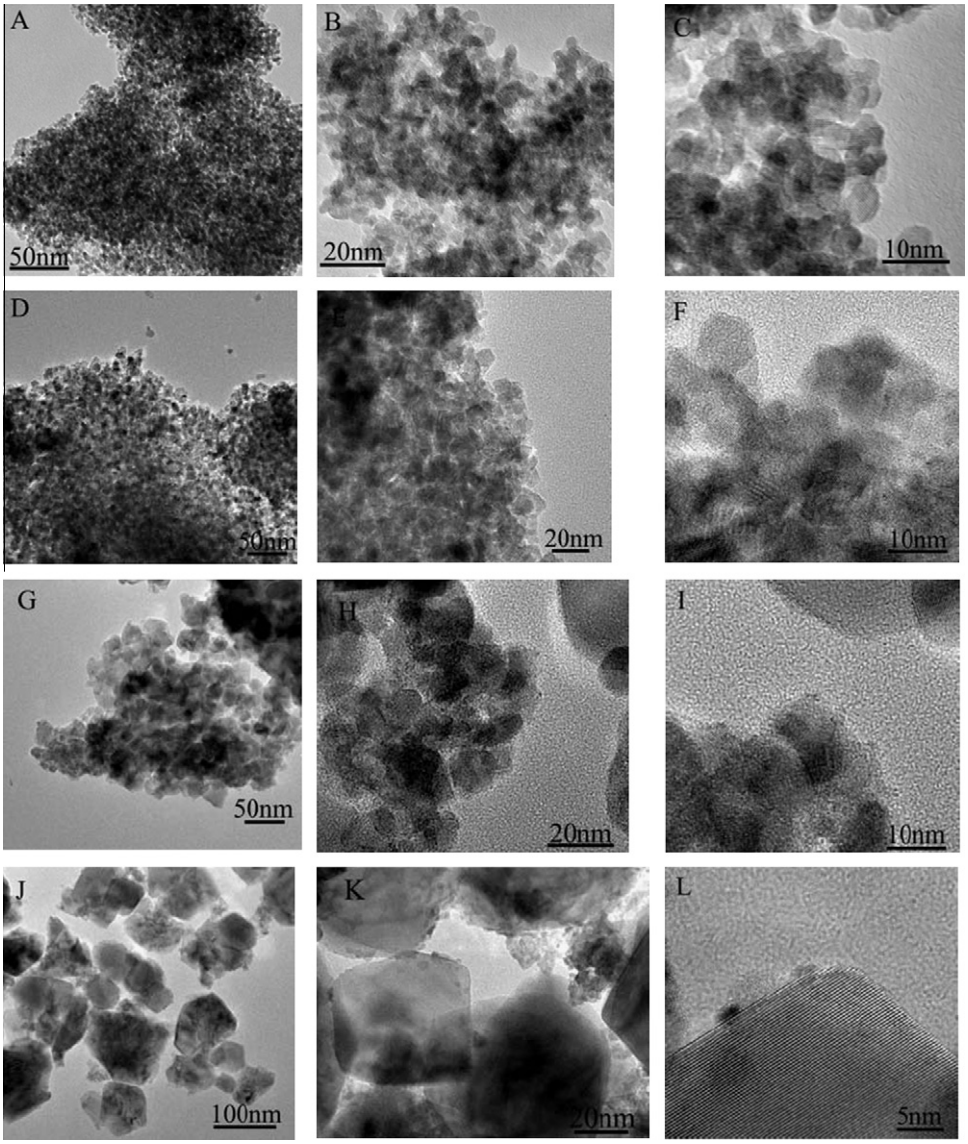

Fig. 1. HRTEM images of the fresh catalysts obtained at increasing magnifications. (A–C) Ir/Ce400. (D–F) Ir/Ce550. (G–I) Ir/Ce700. (J–L) Ir/Ce850.

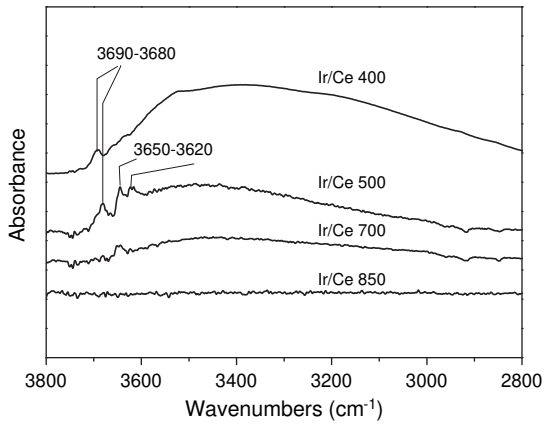

Fig. 2. DRIFT spectra (corresponding to the range of hydroxyl bands) of the catalysts pretreated under air at 400 °C, recorded under flowing Ar (50 mL/min) at 100 °C.

by the presence of the gaseous CO_2 doublet at 2300–2400 cm^{-1}. For the sample calcined at 550 °C, the hydroxyls progressively disappear upon heating, with strong dehydroxylation of the surface observed around 400 °C. Bicarbonates are initially observed in the range of 1400–1650 cm^{-1}; they decompose upon heating to 400 °C. For the Ir/Ce850 sample, practically no hydroxyl or oxygenate bands are observed by infrared analysis over the entire temperature range.

3.1.3. Surface basicity (CO_2 TPD, in situ IR, and microcalorimetry)

The surface basicity of the samples was first investigated by temperature-programmed desorption (TPD) of CO_2. As shown in Fig. 3, three CO_2 desorption peaks, located at about 110, 340, and 700 °C, can be identified. They correspond to weak (denominated LT for low temperature), moderate (MT for medium temperature), and strong (HT for high temperature) basic sites, respectively [25–27].

In line with the *in situ* IR measurements presented above, and in agreement with the literature [28,29], the LT peak can be assigned to the reactive desorption of bicarbonates resulting from the interaction of CO_2 with weakly basic hydroxyl groups on ceria. The MT peak can be assigned to the more stable carbonate species formed from the interaction of CO_2 with surface oxygen atoms of ceria (both mono- and bidentates, depending on the surface coverage and the desorption temperature). The HT peak, above 600 °C, can tentatively be assigned to structural carbonates resulting from the reaction of bulk lattice oxygen with CO_2 [30].

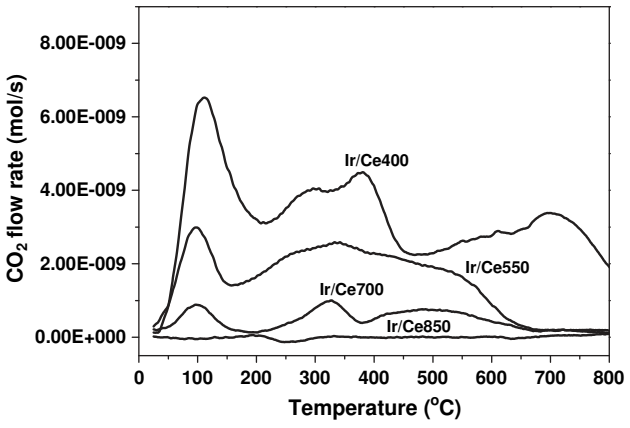

Fig. 3. CO_2-TPD profiles of the catalysts prereduced at 400 °C under flowing H_2 (4 vol% CO_2/Ar, (40 mL/min), heating rate: 10 °C/min).

From the above statements, it can be concluded that a variety of basic sites is present in the high surface-area Ir/Ce400 sample, whereas only sites with weak and moderate basicity exist on the Ir/Ce550 and Ir/Ce700 samples. Almost no surface or bulk basicity is observed for the highly sintered Ir/Ce850 catalyst. By estimating the number of basic sites from the integration of the LT, MT, and HT peaks, it can be seen in Table 2 that the total concentration of basic sites on Ir/Ce400 is almost seven times higher than that on Ir/Ce700. Assuming that most of the desorbed CO_2 originates from the ceria surface sites, the intrinsic surface concentration equals about 1 μmol of basic sites per m^2_{ceria}. This value is quite compatible with the average surface oxygen concentration of 22 μmol/ m^2_{ceria} calculated on the basis of an equal distribution of (1 0 0), (1 1 1), and (1 1 0) planes [22].

The surface basicity was also evaluated in terms of the mean heat of CO_2 adsorption per unit of catalyst mass or per mole of adsorbed CO_2, as reported in Fig. 4. Both the specific heat of adsorption (per kilogram of catalyst) and the mean heat of adsorption per mole of adsorbed CO_2 (Fig. 4, right-hand side) tend to decrease when the surface area is decreased (though this was not calculated for the most sintered sample, Ir/Ce850, because of its weak calorimetric signal). This trend indicates that the mean basic strength per adsorption site regularly decreases as the surface area decreases.

3.1.4. Oxygen storage capacity (OSC) and catalyst reducibility (TPR)

The OSC results reported in Table 3 indicate a marked decrease of the O storage capacity from 1192 Oμmol/g for Ir/Ce400 to 324 Oμmol/g for Ir/Ce850. In order to evaluate the effective amount of O concerned by OSC in the ceria support, the experimental OSC values were corrected for the Ir phase redox contribution. Then, assuming a simple model for ceria surface oxygen atom density (based on an isodistribution of 1 0 0, 1 1 1, and 1 1 0 planes), the number of ceria layers concerned by the OSC was evaluated. As can be seen in Table 3, this number varies only slightly between 1 and 3 ceria layers over the series of catalysts tested, representing only a small percentage (less than 10%) of the total content of O atoms in the ceria. It can be deduced that only surface/subsurface oxygen atoms are available for any redox process for the present series of ceria-based materials.

Fig. 5 shows the TPR profiles for the four catalysts. In the case of the well-dispersed Ir/Ce400 catalyst, the low-temperature peak corresponds to a hydrogen consumption that considerably exceeds that which is necessary for the reduction of the iridium particles. In agreement with the literature, the low-temperature TPR peak can be assigned to both the reduction of the IrO_2 and the partial reduction of the ceria surface [31]. A group of broad TPR peaks was observed in the region from 200 °C to about 400 °C, increasing significantly for the Ir/Ce550 and Ir/Ce700 samples. These TPR peaks can be assigned to the reduction of the surface and of some of the bulk CeO_2 particles (Ce^{4+} to Ce^{3+}) [32,33]. Indeed, according to the literature [34–36], during the TPR of pure ceria, superficial cerium ions are reduced by H_2 at approximately 540 °C. It is generally assumed, however, that the surface reduction of ceria is largely enhanced in the presence of metals. The total hydrogen consumption during the TPR experiment is reported in Table 3. It agrees very well with the OSC data.

3.1.5. Oxygen isotopic exchange (SSITKA)

The oxygen isotopic exchange was investigated by SSITKA in order to evaluate the impact of ceria grain size on oxygen mobility. Fig. 6 shows the typical profiles collected during the $^{16}O_2$-to-$^{18}O_2$ and $^{18}O_2$-to-$^{16}O_2$ switches over the Ir/Ce550, Ir/Ce700, and Ir/Ce850 samples (ensuring a constant total partial pressure of oxygen during the whole transient experiment, *i.e.*, keeping the catalyst under stationary conditions). The duration of the two

Table 2
Basic site concentration obtained from the TPD profiles after CO_2 chemisorption (Fig. 2). ε corresponds to very small and not quantified concentration values for very weak or even non detected peak.

Catalyst	Basic sites I ($\mu mol/g_{cat}$)	Basic sites II ($\mu mol/g_{cat}$)	Basic sites III ($\mu mol/g_{cat}$)	Total basic sites ($\mu mol/g_{cat}$)	Intrinsic basicity ($\mu mol/m^2_{ceria}$)
Ir/Ce400	49	72	54	175	1.1
Ir/Ce550	26	58	ε	84	0.8
Ir/Ce700	6	20	ε	26	0.6
Ir/Ce850	ε	ε	ε	ε	ε

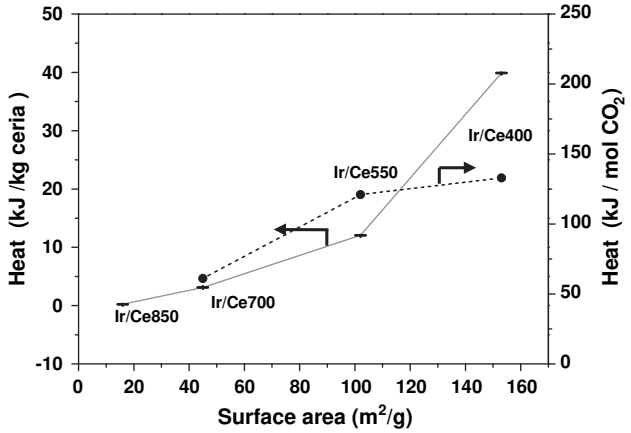

Fig. 4. CO_2 adsorption enthalpy at 30 °C expressed in kJ per kg of catalyst (left hand side) and in kJ per mol of adsorbed CO_2 (right-hand side) as a function of BET surface area. The value in kJ per mol of adsorbed CO_2 corresponding to the Ir/Ce850 sample was not determined due to a too large uncertainty in dividing very low values of adsorption heat and amount of adsorbed CO_2.

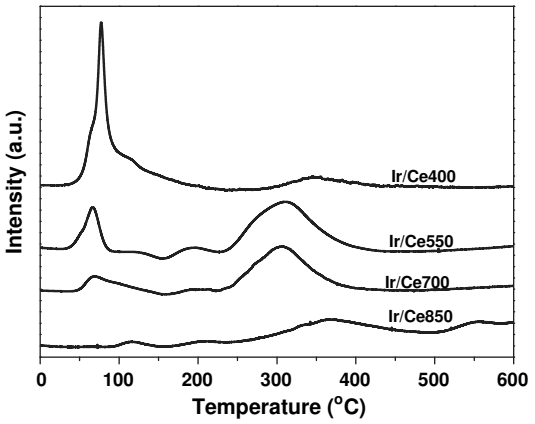

Fig. 5. H_2-TPR profiles of the unreduced catalysts (5 vol%H_2/He 40 mL/min; heating ramp:10 °C/min).

successive switches to $^{18}O_2$ and back to $^{16}O_2$ was about 20 min each, until the outlet signals of the three dioxygen species (unlabeled $^{16}O_2$ at $m/z = 32$, mixed $^{16}O^{18}O$ at $m/z = 34$, and labeled $^{18}O_2$ at $m/z = 36$) were stabilized. During the first switch, the $^{16}O_2$ signal decreases, accompanied by a rise of the $^{18}O_2$ signal, while the $^{16}O^{18}O$ signal passes through a maximum to level off at a value that corresponds to 2% of $^{16}O_2$ present in the $^{18}O_2$ feed. Relaxation curves following the second switch ($^{18}O_2$ to $^{16}O_2$) are essentially identical to those of the first switch, except for the $^{16}O^{18}O$ signal that returns to zero intensity. As can be seen in Fig. 6, the shape of the $^{16}O^{18}O$ signal changes progressively with ceria calcination temperature: for the first transient, the sharp initial part decreases in intensity.

The total number of exchangeable oxygen atoms observed by SSITKA was calculated, after correction for the 2% of $^{16}O_2$ present in the $^{18}O_2$ feed, and is reported in Table 3 as O_{exch}. For the Ir/Ce550 and Ir/Ce700 samples, the number of exchangeable oxygen atoms equals approximately 38% and 37% of the total number of oxygen atoms contained in the catalyst, respectively, accounting for both the ceria phase (11.6 mmol O/g, assuming CeO_2 stoichiometry) and the Ir phase (0.2 mmol O/g). Similar results were reported in [22]. Note that comparable results (though not quantified due to a technical problem during the experiment) are expected for the most-dispersed sample, Ir/Ce400. In contrast, for the most-sintered material (Ir/Ce850), there is a major drop in the percentage of exchangeable oxygen, down to 2%. Though this exchangeable oxygen parameter cannot be directly related to the catalytic process, it probably reflects the strong decrease in the concentration of ceria surface defects which occurs when the surface area has been highly sintered and/or the interface between the Ir and ceria phases has been severely altered, affecting the activation of dioxygen before the further steps of surface migration and bulk exchange throughout the oxide lattice.

Table 3
Oxygen storage and exchange capacity.

Catalyst	S_{BET} (m^2/g_{cat})	OSC_{exp} ($\mu molO/g_{cat}$)	OSC_{Ir} ($\mu molO/g_{cat}$)	OSC_{cor} ($\mu molO/g_{cat}$)	N_{layer}/OSC	H_2 (TPR) ($\mu molH_2/g_{cat}$)	O_{exch} ($mmolO/g_{cat}$)	O_{exch} (%)
Ir/Ce400	153 (61)	1192	200	992	1.2	1195	nd	nd
Ir/Ce550	102 (43)	1128	188	940	1.7	1135	4.5	38
Ir/Ce700	45 (20)	862	195	667	2.7	982	4.3	37
Ir/Ce850	16 (12)	324	182	142	1.6	547	0.2	2

OSC_{exp} = experimental value of oxygen storage capacity.
Osc_{Ir} = contribution from Ir oxydation ($Ir + 2° \rightarrow IrO_2$).
OSC_{cor} = experimental OSC corrected from Ir oxidation,
N_{layer}/OSC = number of ceria layers involved in OSC, assuming (i) a mean ceria surface density of oxygen atoms of 21.7 $\mu molO/m^2$, (ii) an equal distribution of (1 0 0) + (1 1 1) + (1 1 0) planes, and (iii) a fraction of lattice oxygen of 25% concerned by ceria reduction ($CeO_2 \rightarrow Ce_2O_3$).
O_{exch} (in $\mu molO/g_{cat}$) = Exchangeable oxygen concentration determined from SSITKA:
O_{exch} (%): Percentage of exchangeable oxygen calculated by considering the total number of oxygen contained both in ceria (1 g of ceria contains (1/172, 115) = 5,8 mmol of CeO_2 *i.e.*, 11,6 mmol O) and in Ir (OSC_{Ir}).

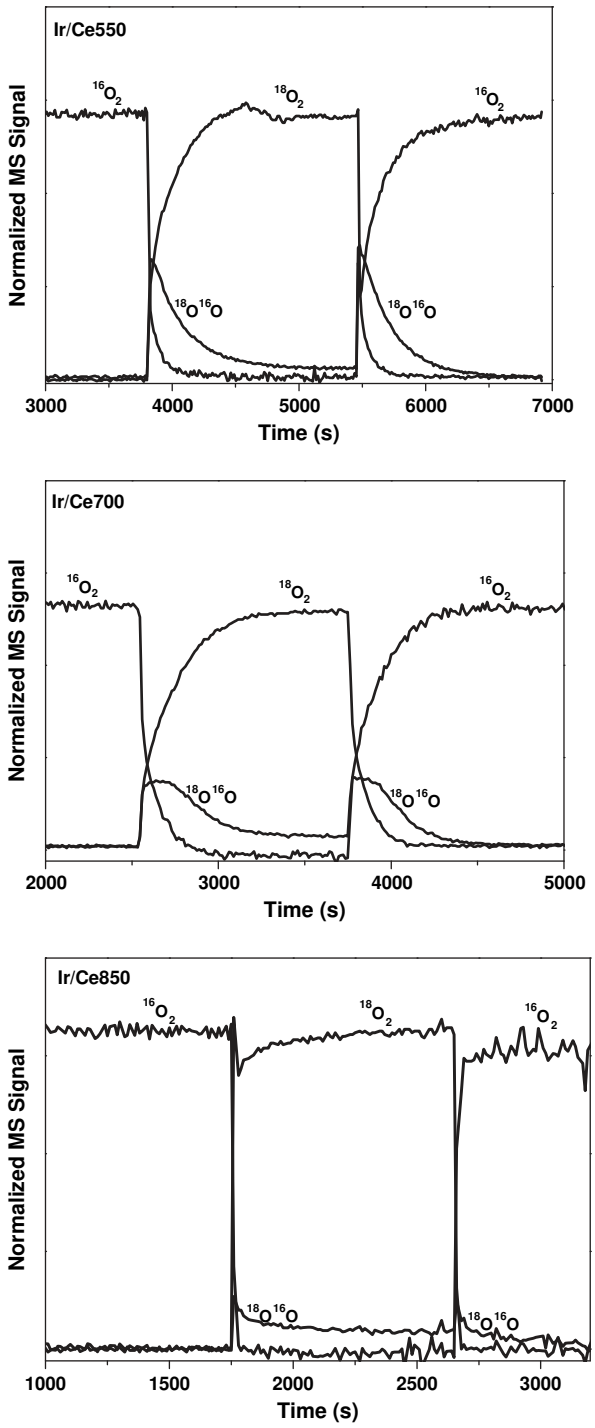

Fig. 6. SSITKA transient curves during forward and backward $^{16}O_2/^{18}O_2$ shift carried out at 650 °C over the Ir/Ce550, Ir/Ce700, and Ir/Ce850 catalysts.

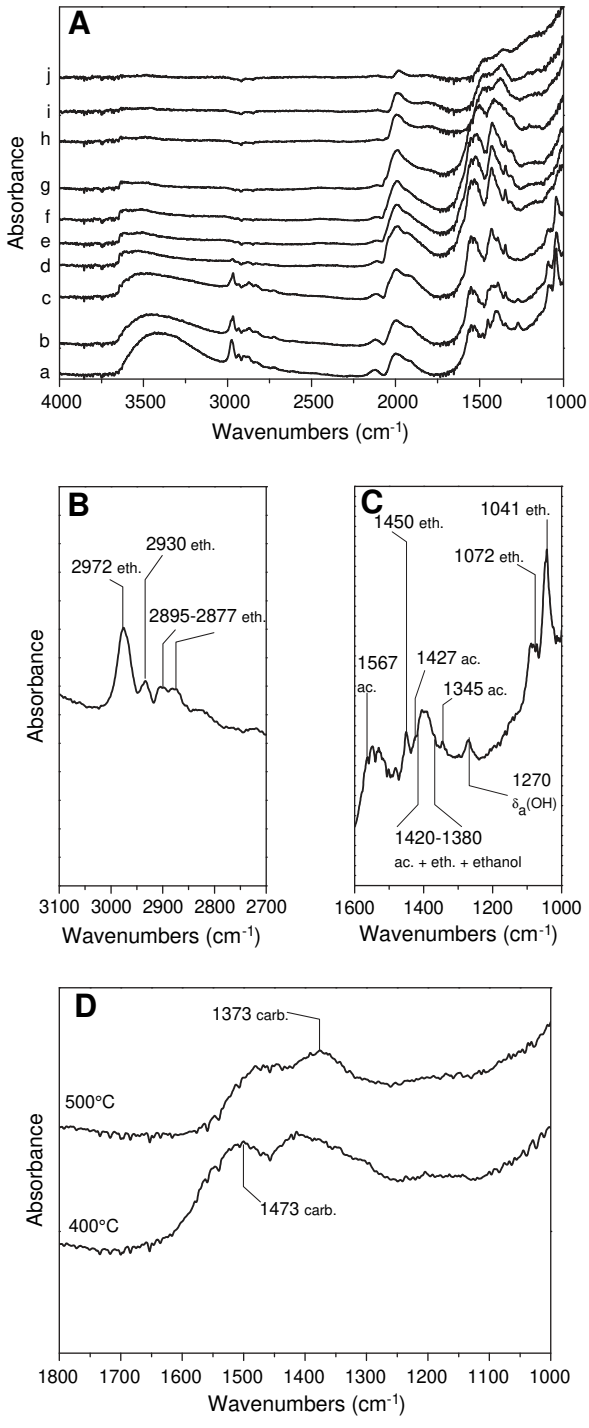

Fig. 7. DRIFT spectra over Ir/Ce550 recorded during ethanol TPD under Ar flow: (A) All spectra (a: 30 °C; b: 100 °C; c: 150 °C; d: 200 °C; e: 250 °C; f: 300 °C; g: 400 °C; h: 500 °C; i: 600 °C; j: 700 °C). (B) Bands assigned to ethoxy species (eth.) in spectrum a. (C) bands assigned to ethoxy species (eth.) and to acetates species (ac.) in spectrum b. (D) bands assigned to carbonate species in spectrum g and h.

3.2. Ethanol decomposition followed by in situ DRIFT under TPD conditions

In order to confirm for this series of catalysts the validity of the ethanol decomposition mechanism already reported for Ir/Ce400 in [17], a DRIFT analysis of ethanol TPD was carried out over the Ir/Ce550, Ir/Ce700, and Ir/Ce850 samples. As seen in Fig. 7A for Ir/Ce550, ethanol adsorbs molecularly at 30 °C. This is based on the observation of the ν(OH) assigned to the broad band located between 3200 and 3600 cm^{-1} and a small negative feature detected at 3676 cm^{-1} that indicates the consumption of basic hydroxyl groups due to molecularly adsorbed ethanol with ceria OH groups [37]. The band attributed to δ_a (OH) of molecularly adsorbed ethanol can be observed at 1270 cm^{-1} (Fig. 7C). The formation of ethoxy species by the dissociation of ethanol is shown by the bands between 2972, 2930, and 2885–2877 cm^{-1}(Fig. 7B), as well as those at 1450 cm^{-1}, 1041 cm^{-1} (bidentate species), and 1072 cm^{-1} (monodentate species) (Fig. 7C), in accordance with

our previous findings in [17] and with the papers of Ozkan [23,24] and Yee et al. [38]. Small bands characteristic of acetate species can already be observed at room temperature at 1567, 1427, and 1345 cm^{-1} (Fig. 7C), as expected from the easy oxidation of ethoxy species into acetate by available surface oxygen, even at low temperature [39]. The bands observed between 2100 and 1800 cm^{-1} are characteristic of the ν(CO) vibrational mode of iridium carbonyl species (Figs. 7 and 8A). It can be noted in Fig. 8A that the distribution of carbonyl species from linear to multi-bonded forms markedly depends on the Ir dispersion: highly dispersed systems (Ir/Ce550) present more multi-bonded carbonyls than more sintered materials (Ir/Ce700), which consistently correspond to differences in activity. This will be discussed later.

The stability of all of these species upon TPD is illustrated in Fig. 8B, which shows that the ethoxy bands tend to vanish at 200 °C, and also that the acetate bands increase up to about 300 °C and decrease between 400 °C and 700 °C. Note that these acetates are progressively replaced by carbonates, which could not be separated from the acetate species in the IR spectra at low temperature, but are revealed at higher temperature (above 400 °C) when the surface is depleted in acetate adspecies (Fig. 7D). The intensity of the bands assigned to CO adsorbed on Ir quite closely follows the changes in the concentration of the acetate/carbonate adspecies. These trends are in full agreement with the sequential scheme proposed previously in [17]: ethanol → ethoxy → acetate → carbonyl species.

In addition, it is strongly suggested that the slow step of the process is related to the formation and diffusion of acetate along the ceria surface, since no delay is observed between the changes in concentration of acetate and carbonyl species. As seen above, the formation of carbonate species essentially above 400 °C when the acetate bands vanish strongly suggests the decomposition of acetates into carbonates. These species might also originate from the readsorption of CO_2 produced, though the latter was not observed as a gaseous product during the ethanol TPD, at variance with the results reported in [24] for cobalt-based materials. No indirect decomposition of ethanol into acetyl species (CH_3CO–) via acetaldehyde formation (1608–1690 cm^{-1}) was observed, as opposed to the results reported in [40]. These intermediates might exist in very low concentration under reaction conditions, since acetaldehyde is a side product, especially at low conversion on highly sintered materials; this will be discussed later.

The DRIFT spectra obtained for Ir/Ce850 were practically free of all the aforementioned adsorption bands during the ethanol TPD. This confirms the quasi-absence of surface defects for adsorbing ethanol as ethoxy adspecies, followed by the oxidation of these adspecies into acetate, which is further decomposed into Ir carbonyls after migration over the surface. This corresponds to the poor reactivity observed in OSR and to the strong selectivity to formaldehyde described later. It can therefore be stated that the ethanol partial oxidation to formaldehyde occurs essentially on a defect-free surface, with no mobility, as observed for this highly sintered sample.

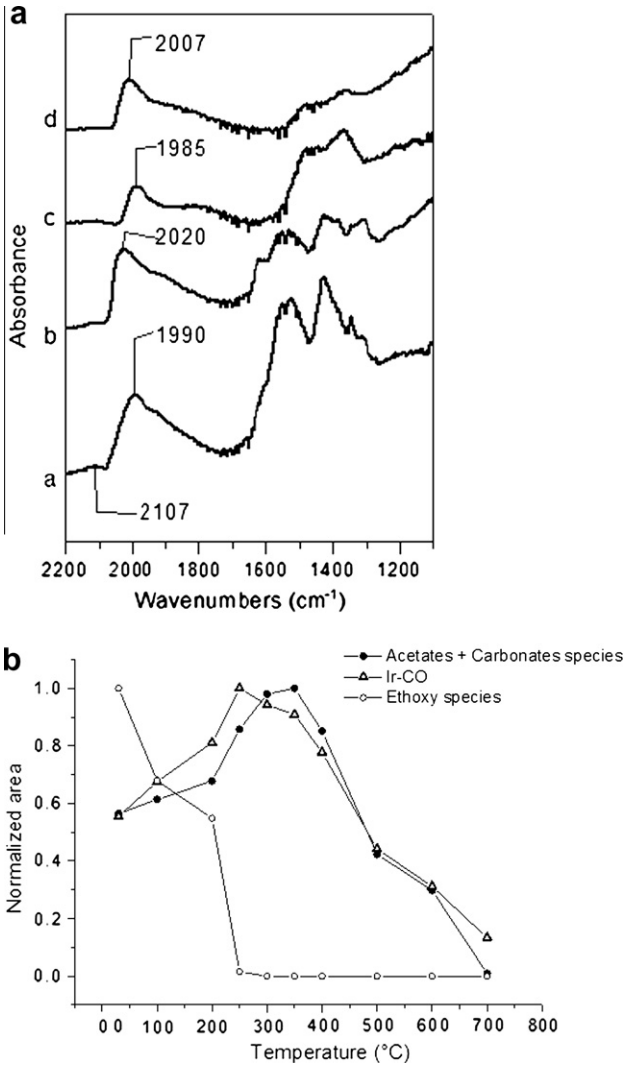

Fig. 8. (A) DRIFT spectra over Ir/Ce550 and Ir/Ce700 recorded during ethanol TPD under airflow: a: Ir/Ce550 at 300 °C; b: Ir/Ce750 at 300 °C; c: Ir/Ce550 at 600 °C; d: Ir/Ce750 at 600 °C. (B) Changes in the integrated absorbance of the ethoxy (3042–2789 cm^{-1} + 1140–990 cm^{-1}), surface acetate/carbonate (1650–1231 cm^{-1}), and Ir carbonyl (2183–1720 cm^{-1}) DRIFT bands as a function of ethanol desorption temperature over Ir/Ce550.

3.3. Product distribution and ethanol conversion at thermodynamic equilibrium

For further comparison with the experimental data, Fig. 9 shows the distribution of the product concentrations calculated at thermodynamic equilibrium (minimizing the Gibbs free energy). Ethanol and oxygen are completely converted over the entire temperature range. The hydrogen concentration increases and reaches a maximum around 700 °C, which coincides with the total disappearance of methane. The CO_2 concentration shows a maximum at approximately 400 °C and steadily decreases at higher temperature. While methane formation also passes through a maximum

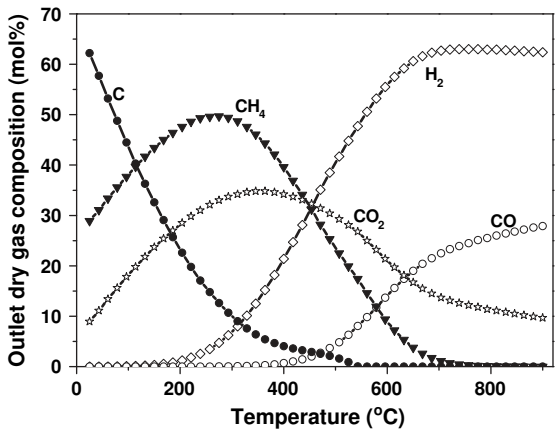

Fig. 9. Thermodynamic equilibrium concentrations for the ethanol oxidative steam reforming as a function of temperature ($EtOH/H_2O/O_2$ = 1/1.8/0.6, pressure: 1 atm).

around 300 °C, CO develops only at higher temperature, as expected from the displacement of both the methanation/methane reforming and the WGS/RWGS equilibrium.

$$CO + 3H_2 \leftrightarrows CH_4 + H_2O \quad (4)$$

$$CO + H_2O \leftrightarrows CO_2 + H_2. \quad (5)$$

No C_2 products are predicted, as they are not thermodynamically stable. Coke formation for the OSR reaction is favored at low temperature (below 200 °C) but hindered above 400 °C.

3.4. Ethanol OSR in the absence of catalyst (blank test)

The non-catalytic gas-phase oxidative steam reforming of ethanol was investigated in the absence of catalyst (Fig. 10). Ethanol progressively decomposes at temperatures higher than 450 °C, reaching a conversion of 90% at 700 °C when the conversion of oxygen is complete. As expected for gas-phase decomposition reactions, a high concentration of CO is observed (about 40% above 500 °C). The hydrogen concentration, however, remains very low (about 10%) because of the high selectivity toward hydrogenated products such as methane and ethylene.

Though the exact contribution of the gas-phase processes under effective catalytic conditions (*i.e.*, in the presence of a catalyst) cannot strictly be deduced from these blank experiments, the next section will clearly demonstrate that the surface reactions are considerably faster and more selective than those of the gas phase.

3.5. Catalytic performances in the oxidative steam reforming of ethanol

3.5.1. Activity and selectivity

Fig. 11 shows the evolution of the conversion and the product concentration as a function of the reaction temperature for the Ir/CeO_2 catalysts investigated. As shown in the upper part of the figure, the Ir/Ce400, Ir/Ce550, and Ir/Ce700 catalysts exhibit similar activity profiles. The conversion of ethanol is complete above 450 °C, and the concentration of hydrogen increases progressively with temperature. By contrast, the ethanol conversion and the hydrogen concentration are significantly lower for the Ir/Ce850 sample. As for the formation of methane and carbon monoxide (central part of Fig. 11), the three most active catalysts exhibit comparable performances as a function of temperature, with decreasing CH_4 production and increasing CO formation. The least active catalyst tends to behave in the opposite way, probably

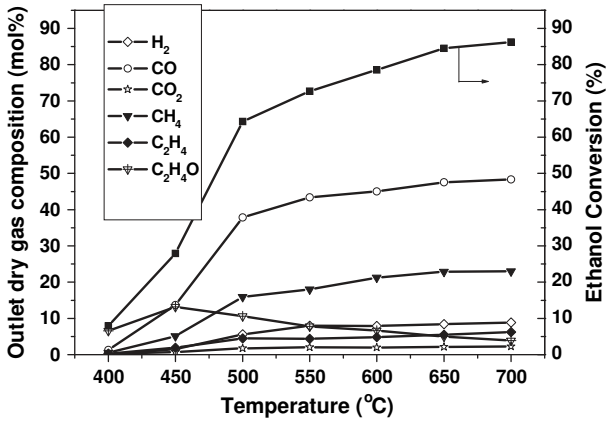

Fig. 10. Conversion of ethanol and outlet gas composition versus temperature in the absence of catalysts. (F_{react}/W_{cat} = 6000 mL g_{cat}^{-1} h^{-1}. Ethanol/H_2O/O_2 = 1/1.8/0.6, W_{cat}: catalyst weight, F_{react}: reactant flow rate).

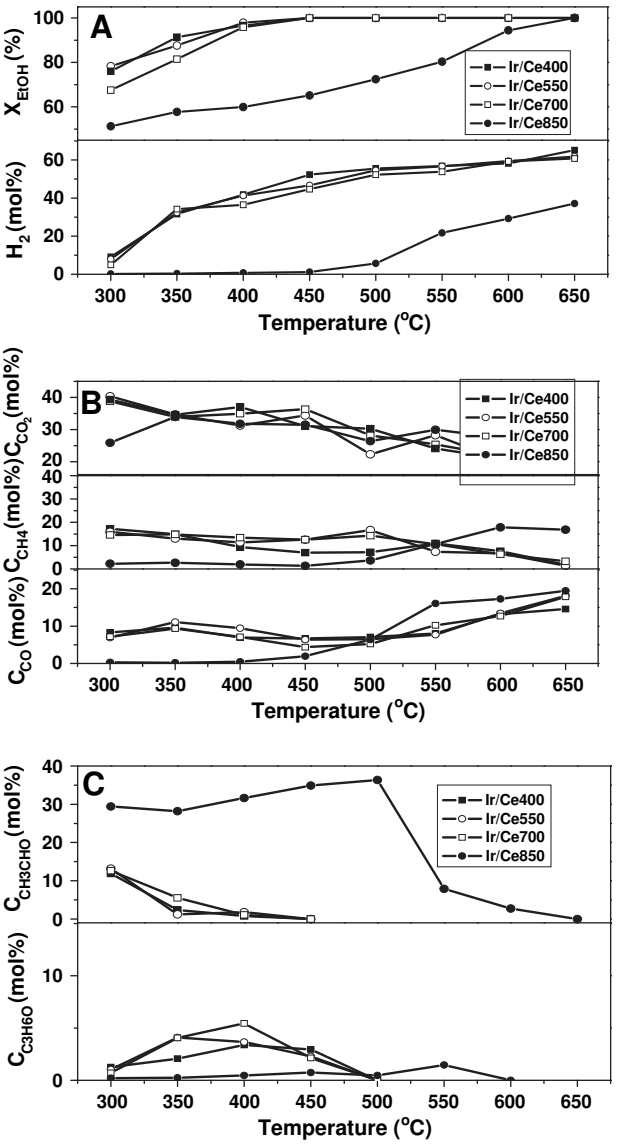

Fig. 11. Effect of reaction temperature on the product distributions for OSR of ethanol in the presence of catalysts. Ethanol/H_2O/O_2 = 1/1.8/0.6, F_{react}/W_{cat} = 6000 mL g_{cat}^{-1} h^{-1}. W_{cat}: catalyst weight, F_{react}: reactant flow rate.

reflecting a significant contribution of the gas-phase decomposition reactions (see blank experiments above) to the overall reaction. In addition, while the three active catalysts exhibit low selectivity toward the undesirable byproduct acetaldehyde (CH_3CHO), the Ir/Ce850 catalyst shows a much higher CH_3CHO formation (bottom part of Fig. 11). Only trace amounts of acetone were formed for this sample. It was also confirmed, by varying the contact time, that the selectivity toward oxygenates remains highest for the Ir/Ce850 catalyst, even at conversion values close to those measured for the other systems (*e.g.*, a selectivity to acetaldehyde of 28% and 10% for a conversion of 55% and 60% is obtained at 300 °C for the Ir/Ce850 and Ir/Ce700 catalysts, respectively).

3.5.2. Stability

The catalytic performance was also investigated for the four catalysts as a function of time onstream over a period of 60 h, at 650 °C, as depicted in Fig. 12. The Ir/Ce400 and Ir/Ce550 catalysts showed full ethanol conversion without significant change in the

product distribution during the entire testing period. Full conversion is not proof that catalyst deactivation does not occur. These conditions were, however, used to discriminate between more stable catalysts (without apparent deactivation) and less stable catalysts (with observed deactivation).

For the Ir/Ce700 catalyst, ethanol was also completely converted during the full duration of the aging test. That said, although no change in the molar distribution of the main products was noted during the first 45 h onstream (59% H_2, 19% CO_2, 17% CO, and 5% CH_4), the concentration of hydrogen decreased gradually to 50% after this time, with a simultaneous increase in the carbon monoxide and methane concentrations. These trends indicate a slight decrease in the activity for methane steam or dry reforming and WGS contributions after an initial stable period.

On the other hand, the Ir/Ce850 catalyst exhibited lower stability, as expressed by a decline in the conversion of ethanol from 100% to about 95% in 60 h, accompanied by the production of undesirable products (about 1–2% acetaldehyde and 2–3% ethylene) in the effluents after about 10 h onstream. In parallel, the hydrogen concentration declined continuously from 40% to 24%, while the concentration of carbon monoxide and methane increased steadily. These trends indicate that the WGS and methane-reforming reactions were more and more inhibited as a function of time onstream.

3.6. Catalyst characterization after long-term aging tests

3.6.1. Morphological changes (XRD and HRTEM)

As with the fresh catalysts, only the XRD diffraction lines characteristic of the CeO_2 fluorite structure were observed on the used catalysts, after the aging tests carried out at 650 °C for 60 h. The ceria grain size increased, however, and the BET surface area decreased significantly, as shown in Table 1 (values in parenthesis). The HRTEM images of the used catalysts (Fig. 13) provide further evidence for the increase in the ceria grain size for all the catalysts in a range similar to that of the XRD measurements. In addition, it was possible to evaluate the mean size of the Ir particles observed on these images and therefore to monitor the changes in Ir dispersion upon aging (see Table 1, data in parentheses). As can be seen, the sintering of Ir particles upon aging tends to be inversely proportional to the initial metal dispersion: sintering is weak on the well-dispersed Ir/Ce400 sample, becoming more and more significant as one approaches the poorly dispersed Ir/Ce850 sample.

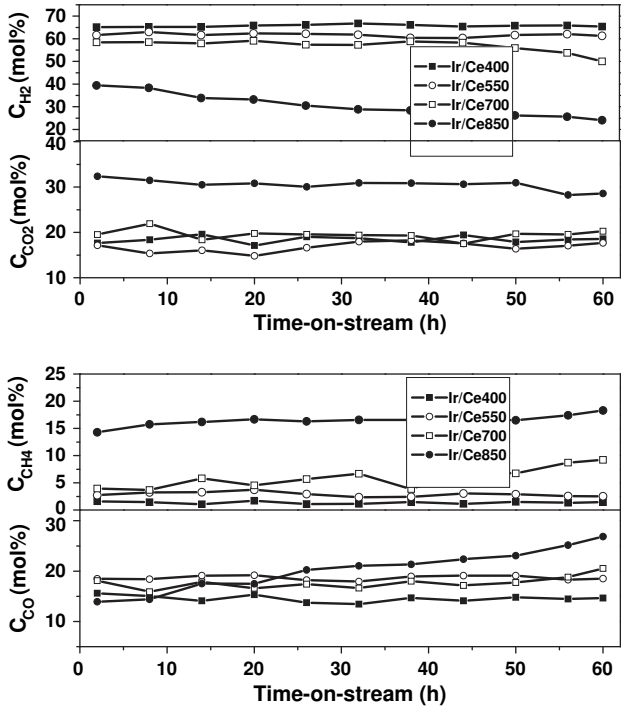

Fig. 12. Changes in outlet gas composition for oxidative steam reforming of ethanol in the presence of catalysts. Reaction conditions: ethanol/H_2O/O_2 = 1/1.8/0.6, temperature: 650 °C, F_{react}/W_{cat} = 6000 mL g_{cat}^{-1} h^{-1}. W_{cat}: catalyst weight, F_{react}: reactant flow rate.

3.6.2. Coke deposition (HRTEM and TPO)

While HTREM yields no evidence of carbonaceous deposits for the two aged Ir/Ce550 and Ir/Ce400 catalysts, a thin layer of encapsulating coke is observed around the Ir/Ce700 catalyst (Fig. 13H). Furthermore, two types of carbon species are observed for the Ir/Ce850 catalyst: a carbonaceous layer on the surface of the grains (Fig. 13K) and filaments (Fig. 13L).

The coke buildup occurring during the long-term aging tests was followed by TPO experiments. Fig. 14A reports the TPO profiles and Fig. 14B the total amounts of coke measured for each aged catalyst. As shown in Fig. 14A, two separate domains of carbon oxidation were clearly observed, each of them being sensitive to the catalyst morphology.

In the low-temperature domain (250–400 °C), at least three types of easily oxidized carbon deposits were detected, while only one TPO peak was detected in the high-temperature domain (above 600 °C). According to the literature [41,42] and our own analysis, the following assignments can be proposed: (i) the lowest-temperature peaks (below 300 °C) correspond to carbonaceous deposits in direct contact with the metallic particles (atomic carbon on Ir particles); (ii) the peaks at intermediate temperature (between 300 and 400 °C) are assigned to carbonaceous deposits at the metal-support interface or on the support in close vicinity of the active metal; and (iii) in the high-temperature domain (above 600 °C), the TPO peak corresponds to stable "hard" coke that encapsulates the catalyst particles. This coke might originate from the polymerization of ethylene formed by undesirable side reactions.

As shown in Fig. 14A and B, the aged Ir/Ce400 catalyst accumulated only a very small amount of highly reactive type (i) carbon. Both Ir/Ce550 and 700 samples yielded TPO traces with essentially medium-temperature peaks corresponding to type (ii) carbon deposits, in a slightly larger quantity (up to three times more for Ir/Ce700). In contrast, the aged Ir/Ce850 catalyst exhibited more than four times more carbon formation than did the Ir/Ce700 catalyst, essentially as type (iii) hard coke deposits. This feature agrees with the HRTEM results reported above.

4. Discussion

In order to determine whether or not ethanol OSR is structure- or texture-sensitive, the reaction has to be investigated over a series of catalysts offering a wide variety of intrinsic properties (surface dynamics, basicity, structure and texture, support and metal dispersion, and so on). Before analyzing the data collected, let us first summarize the main features of the ethanol OSR mechanism over Ir/CeO_2 catalysts, as already described in [16,17].

4.1. Main mechanistic features of ethanol OSR

From the present operando DRIFTS investigation and in line with our mechanistic approach already presented in [17], it is proposed that gaseous ethanol adsorbs via dissociative adsorption onto the ceria surface at defect sites (oxygen vacancies associated with basic OH groups) to generate ethoxy intermediates. The

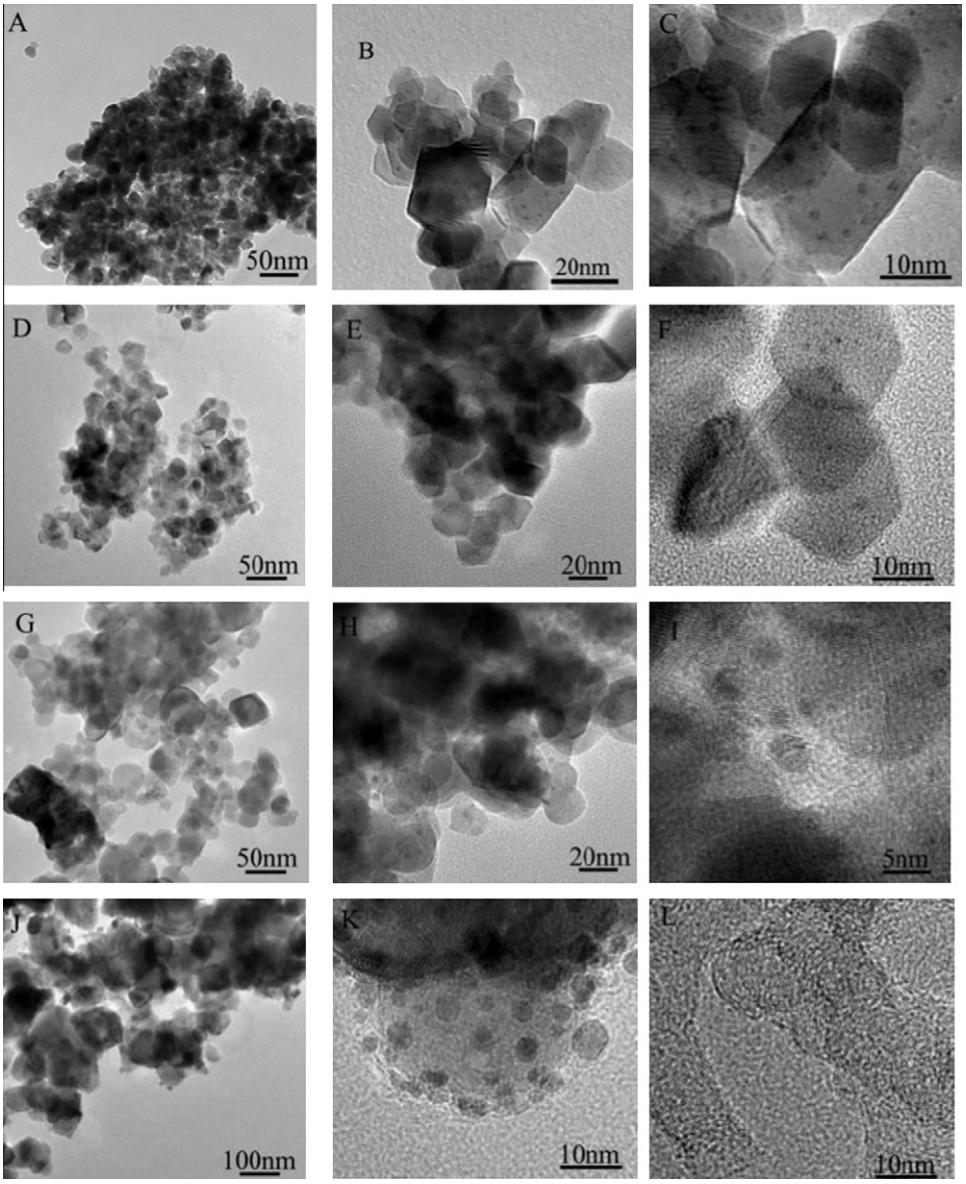

Fig. 13. HRTEM images of the Ir/CeO_2 catalysts used for OSR reaction. (A–C) Ir/Ce400. (D–F) Ir/Ce550. (G–I) Ir/Ce700. (J–L) Ir/Ce850. Reactions at 650 °C for 60 h onstream, Ethanol/H_2O/O_2 = 1/1.8/0.6, $F_{react}/W_{cat} = 6000$ mL g_{cat}^{-1} h^{-1}.

ethoxy species can be directly oxidized into acetate species by using ceria surface oxygen or dehydrogenated into acetaldehyde, which may subsequently react with hydroxyl groups (produced from water dissociation on the ceria defects) to form acetate adspecies, together with the elimination of H_2 [24]. Like the hydroxyl groups, the acetate adspecies can migrate along the ceria surface via the aforementioned defect sites, and therefore approach the Ir/ceria interface, likely due to local gradient concentrations around the Ir particles. Here, the acetate species can readily decompose into C_1 adspecies to form (i) metal carbonyl groups, possibly via methyl groups bonded to the Ir particles and (ii) carbonate species remaining at the Ir/ceria interface. During this sequential oxidation process, the oxygen adspecies required to regenerate the reduced ceria defect sites are provided from gaseous oxygen dissociation on the Ir surface and/or by the ceria interfacial sites (OH and decomposing carbonates). In parallel, side processes occurring essentially on the ceria surface might involve ethoxy dehydroxylation into acetyl species immediately desorbed as acetaldehyde and/or ethanol dehydration into ethylene. Sequential processes involving both ceria and metal sites were also proposed in [5,15,43] on other types of catalysts, though not as fully described as in this work and also with variations in the ceria-based steps.

The active sites participating in the ethanol OSR mechanism on Ir/ceria catalysts can therefore be classified as: (i) the ceria surface oxygen vacancies associated with basic hydroxyl groups, where the ethanol adsorption, partial oxidation into acetate, and surface diffusion toward the Ir particles occur; (ii) the metal-support interfacial sites where the C–C dissociation of the acetate adspecies proceeds; and (iii) the Ir surface atoms, which permit the dissociation and spillover of oxygen toward the ceria, carbonyl formation, and CO desorption.

Other mechanistic routes dealing essentially with metal chemistry have been proposed for specific cases such as evaporated metal films [44,45]. These routes are not considered in the present study, since the probability that an ethanol molecule will collide with a metal particle is marginal compared with the likelihood of collision with ceria, even for the sample displaying a low ceria

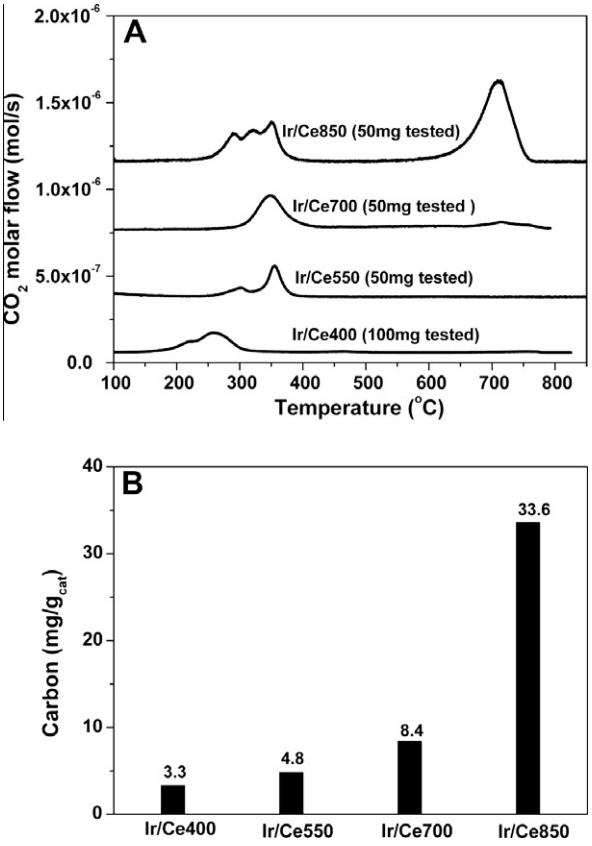

Fig. 14. Temperature-programmed oxidation of the used catalysts after ethanol oxidative steam reforming at 650 °C for 60 h onstream. Ethanol/H_2O/O_2 = 1/1.8/0.6, $F_{react}/W_{cat} = 6000$ mL g_{cat}^{-1} h^{-1}. W_{cat}: catalyst weight, F_{react}: reactant flow rate. (A) TPO profiles. (B) Total amount of deposited carbon.

surface area and low Ir dispersion. In addition, the strong influence of the ceria surface and structure, which will be demonstrated later, also supports the non-retention of mechanisms restricted to the metal surface for the present case study.

4.2. Textural and morphological effects on the surface dynamics (diffusion of oxygenated and hydrogen adspecies) during the ethanol conversion process

The mechanism proposed above for ethanol OSR involves the diffusion of several adspecies on the ceria surface from or to the Ir particles. The question arises as to which surface characteristics control the diffusivity factor.

4.2.1. Role of Ir/ceria interface

As seen above, the Ir/ceria interface permits the cracking of C_2 adspecies into C_1 species. It may also be crucial for the spillover of activated hydrogen or oxygen from Ir to ceria during the reduction and catalytic steps, respectively. In Table 4, we have calculated and reported the intrinsic length of the peripheral interface between the Ir particles and the ceria support (IP, expressed in m_{Ir}/m^2_{ceria}) for all solids tested, before and after long-term testing. This was calculated by assuming a simple hemispherical model for the metal particles as reported in [46]. This structural parameter, which depends on both Ir dispersion and ceria surface area, varies in a limited range over the series of tested catalysts and will be used later for calculating specific turnover frequency (TOF) values and identifying possible structure sensitivity at the metal/support interface.

Let us now consider the TPR results reported in Fig. 5. In noble metal/CeO_2 catalysts, dihydrogen, once dissociated on noble metal, is able to spillover onto the CeO_2, which favors the reduction of Ce^{4+} at the surface of the support [47]. Here, it is observed that the reduction process is strongly hindered for sintered materials, leading to a much lower reduction of the ceria (surface and bulk) as shown by the shift of TPR peaks to higher temperatures and lower intensities. This observation suggests that a drastic change occurs in the Ir–Ce interaction (nature and/or concentration of interfacial sites) when the ceria and the iridium are sintered. Since it was shown in Table 4 that the concentration of the peripheral sites did not change to a great extent, it can be inferred that essentially the nature of the interface sites changes upon the sintering of both metal and support. This could be directly related to the changes in the structure of the Ir particles (*e.g.*, the concentration of coordinately unsaturated sites, CUSs, as commonly accepted for noble metal particles [48]) and of the ceria surface (*e.g.*, defect density) over the series of materials tested.

4.2.2. Effect of ceria defect density

It is generally agreed that the defect density in ceria-based catalysts affects the oxygen mobility, as reflected from OSC and isotopic exchange kinetics. The mobile oxygen species in ceria are, thus, essentially interstitial oxygen ions preferentially located at fluorite structure defects [49]. From the OSC measurements reported in Table 3, one to three ceria monolayers are concerned under OSC redox conditions. In Fig. 15, it can be seen that the concentration of reducible oxygen corresponding to these OSC measurements (Fig. 15A) and the concentration of exchangeable oxygen derived from SSITKA (Fig. 15B) can be ranked in a manner similar to the intrinsic conversion of ethanol (Fig. 15D) as a function of the surface area, namely Ir/Ce400 ≈ Ir/Ce550 > Ir/Ce700 ≫ Ir/Ce850. This statement indicates that the concentration of defects, associated with the concentration of reducible and exchangeable oxygen,

Table 4
Advanced description of the catalyst surface in term of Ir particle concentration (N_{Ir}) and length of peripherical interface between the Ir particles and the ceria support (IP).

Catalyst	x_{Ir} (wt.%)	d_{Ir}[a] (nm)	D_{Ir}[b] (%)	S_{BET}[c] (m^2/g_{cat})	N_{Ir}[d] (10^{15} particles/m^2)	Δ[e] (nm)	IP[f] a
Ir/Ce400	1.92	1.4 (1.5)	67 (61)	153 (61)	2.0 (4.2)	21 (22)	3.6 (7.4)
Ir/Ce550	1.81	1.5 (2.0)	62 (46)	102 (43)	2.3 (2.3)	19 (19)	4.3 (6.0)
Ir/Ce700	1.87	1.6 (2.5)	59 (37)	45 (20)	4.5 (2.5)	13 (22)	9.2 (8.3)
Ir/Ce850	1.75	3.5 (4.0)	26 (23)	16 (12)	1.1 (1.0)	26 (27)	4.7 (5.4)

[a] d_{Ir} = mean Ir particle size before and after long-term runs.
[b] D_{Ir} = Ir dispersion before and after long-term runs.
[c] BET surface area before and after long-term runs.
[d] Intrinsic number of Ir particles calculated from x_{Ir} = content of Ir (%), d_{Ir} = mean Ir particle size (nm), ρ = metal density (22.562 g/cm^3), and S_{BET} = surface area (m^2/g_{cat}) according the formula: $N = 10^{19} x_{Ir}/d_{Ir}^3 \rho S_{BET}$.
[e] Mean inter particles distance calculated from $\Delta = \left(\frac{1}{N_{Ir}}\right)^{0.5} - d_{Ir}$.
[f] Intrinsic perimeter of contact between Ir particles and ceria grains, calculated from $IP = \beta s_{IR} D_{Ir}^2/S_{BET}$ with β a shape factor based on an hemispheric interfacial perimeter of Ir particles over the ceria surface (= 6.35×10^5 m/g_{Ir}), x_{Ir} the Ir content, D_{Ir} the Ir dispersion.

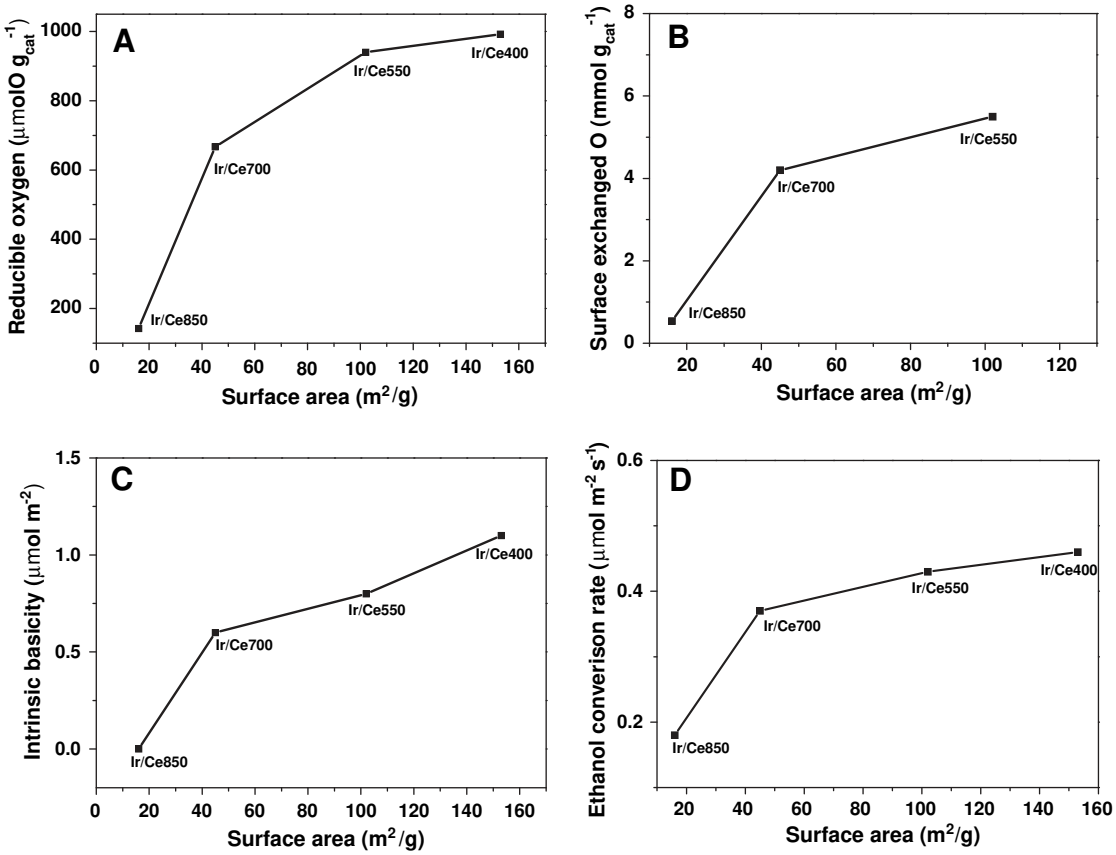

Fig. 15. Concentration of ceria reducible oxygen species under OSC conditions (A), exchangeable oxygen calculated from the $^{16}O^{18}O$ SSITKA (B), intrinsic basicity calculated from CO_2 TPD (C), and intrinsic rate of ethanol conversion (D) as a function of catalyst surface area.

plays a major role in the overall OSR process. A similar conclusion was obtained for Ni/Y_2O_3 by Sun et al. [50].

Let us now see whether this characteristic can also be described in terms of surface basicity.

4.3. Textural and morphological effects on surface basicity

Changes in surface basicity as a function of ceria surface area are illustrated in Fig. 15C (from CO_2 TPD results). They clearly indicate a large decrease in site concentration upon ceria sintering, closely following the changes in intrinsic conversion of ethanol (Fig. 15D).

Changes in the CO_2 heat of adsorption measured by calorimetry (Fig. 4) show in addition that the basicity decreases not only in basic site concentration (left hand side) but also in terms of surface basic strength (right-hand side) upon sintering. Accordingly, the highly sintered catalyst (Ir/Ce850) displays a very low concentration of weak basic sites compared to the other catalysts.

This change in surface basicity was also reflected by DRIFT investigations (Fig. 2) that showed a progressive decrease in the basic hydroxyl group concentration upon ceria sintering.

Similar trends are therefore observed for the changes in concentration of exchangeable oxygen indirectly related to surface defects, in surface basicity (concentration and strength) and in intrinsic rate of ethanol conversion upon ceria sintering. In line with the main mechanistic steps of ethanol OSR, this decrease of the surface basicity (hydroxyl groups and oxygen defects) would hinder the diffusion of C_2 intermediates toward the Ir–Ce interface and their further decomposition into C_1 products, as deduced from the much favored formation of oxygenates, like acetaldehyde, over the highly sintered Ir/Ce850 catalyst. Another consequence is that other routes, such as dehydration into ethylene, also become favored on the less basic systems, provoking further polymerization into coke, as also observed for the Ir/Ce850 sample (*e.g.*, 2–3% of ethylene was formed for Ir/Ce850 but less than 1% for the three other samples).

4.4. Relation of the intrinsic activity to the catalyst morphology and structure

In order to identify the role played in the intrinsic activity by the morphology and/or the structure of the catalysts – in other words, the possible structure sensitivity of ethanol OSR – we have successively considered the various types of active sites that are involved in the bifunctional mechanism described above, calculating for each one a turnover frequency (or TOF) in mole of ethanol converted per mole of active site per second. The sites considered were as follows: (i) the reducible ceria oxygen atoms (the concentration of which is derived from the OSC value of the ceria grains, OSC_{cor}, in Table 3), (ii) the Ir surface atoms (the concentration of which is obtained from Ir dispersion, D_{Ir}, in Table 4), and (iii) the Ir–Ce interface sites (the concentration of which is based on the length of peripheral interface between the Ir particles and the ceria support (IP in Table 4).

These values are reported in Table 5. The chosen reaction temperature was 300 °C, in order to make these calculations under conditions leading only to partial ethanol conversion for all catalysts, as can be verified in Fig. 11. As can be seen, for each type of active site considered, there is a significant decrease in the TOF values over the series of catalysts from the well-dispersed Ir/Ce400

Table 5
Specific and intrinsic rates and turn over frequency values calculated by considering three different types of potentially active site: reducible ceria surface oxygen, surface Ir atom and Ir/ceria interface site. The reaction temperature is 300 °C, under the conditions corresponding to Fig. 11.

Catalyst	S_{BET} (m^2/g_{cat})	d^d_{Ir} (nm)	d^d_{CeO2} (nm)	μmol EtOH/g_{cat} s	μmol EtOH/m^2 s	TOF per reducible O_{surf} s^{-1}	TOF per Ir_{surf} s^{-1}	TOF per $Ir_{interface}$ s^{-1}
Ir/Ce400	153	1.4	6	70	0.46	0.09	1.0	2.0
Ir/Ce550	102	1.5	8	44	0.43	0.08	0.5	1.6
Ir/Ce700	45	1.6	15	17	0.37	0.07	0.3	0.7
Ir/Ce850	16	3.5	44	3	0.18	0.03	0.1	0.6

to the poorly dispersed Ir/Ce850. Globally, this trend confirms the structure sensitivity of the reaction.

Now, for a deeper insight into this phenomenon, each TOF value must be related to the concentration of the active site considered. Accordingly, the TOF per ceria surface active site (regarded as the reducible oxygen atoms) has to be related to the size of the ceria grains, as shown in Fig. 16A. The TOF per Ir surface atom has to be related to the size of the Ir particles, as shown in Fig. 16B. For the TOF calculated per Ir–ceria interfacial site, we consider both the Ir particle size and the ceria grain size, as depicted in Fig. 16C.

4.4.1. TOF calculated per active ceria site

This TOF value regularly decreases as the ceria grain size increases (Fig. 16A). This observation conclusively confirms that the process steps starting with ethanol adsorption up to acetate migration toward the Ir particles are controlled by the state of the ceria surface, which is determined by the size of the grains. Based on the information collected in this study, this relationship should emanate directly from the density of surface defects (OH groups associated with oxygen lattice), which is also described by the surface basicity.

It can also be of interest to evaluate the characteristics of surface diffusion during the OSR steps occurring over the ceria surface. Let us first assume a mean diffusion coefficient $D_s = 10^{-18}$ m^2/s, as derived from the literature for hydroxyl species [51], to represent the mobility of the various reacting adspecies (essentially OH, ethoxy, and acetates), moving over the ceria surface from the ceria landing sites toward the Ir particles. If one bases reacting times on the TOF values ($\tau = TOF^{-1}$) related to the ceria contribution, one obtains a mean diffusion distance of about 4 nm, calculated from

$$L\ (\mathrm{nm}) = 10^9 \sqrt{D_s \tau}$$

Now, this diffusion distance should be compared with the mean distance between two adjacent Ir particles. A simple model was used to evaluate this mean distance (Δ) for the various catalysts studied, as reported in Table 4. As can be seen, these Δ values remain within a range of 13–27 nm, over the whole series of samples.

By considering a ceria landing site for ethanol adsorption between two Ir particles, the largest distance to reach an Ir particle for an intermediate species will be $\Delta/2$, *i.e.*, about 10 nm.

This simple surface dynamic modeling shows that the diffusion distance of a reacting intermediate over the ceria surface is of the same order of magnitude as the distance required for this intermediate to reach an Ir particle for further cracking steps. This indicates that the process steps dealing with the ceria surface (ethanol adsorption, partial oxidation, and diffusion) are kinetically controlled by the surface diffusion. In the higher temperature range (600–700 °C) where the long-term tests were performed, this kinetic feature is even more valid, since OSR is much more activated (by a factor of two or three) compared to the surface diffusion.

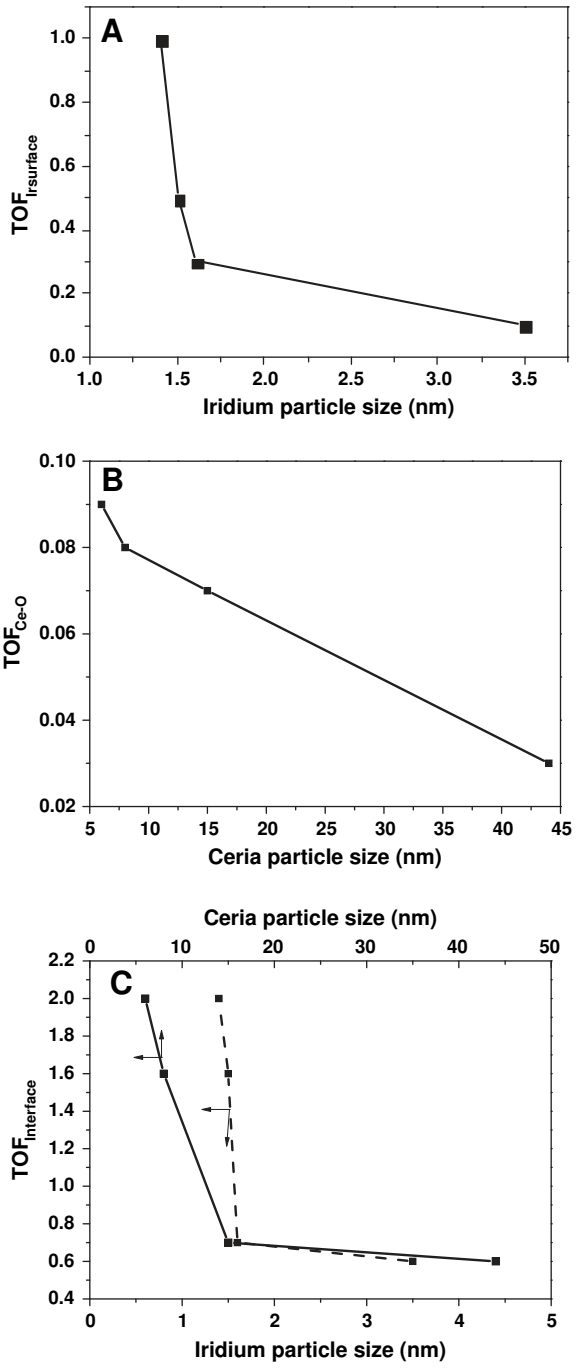

Fig. 16. TOF values calculated according to the concentration of surface atoms of Ir particles (A), ceria reducible oxygen atoms (B), and interfacial Ir–ceria sites (C) as a function of Ir particle size (A and C) and ceria grain size (B and C). Experimental conditions: temperature = 300 °C, $F_{react}/W_{cat} = 72,000$ mL g_{cat}^{-1} h^{-1}.

4.4.2. TOF calculated per surface atom of iridium

As seen previously for the ceria TOF, the Ir TOF also decreases when the Ir particle size increases, but in a non-linear fashion (Fig. 16B). A strong decrease occurs in the domain of the small particles (ranging from about 1.5 to 2 nm), while the decrease becomes much less severe for larger particles (up to 3.5 nm in the figure). This trend is confirmed by considering a TOF value below 0.1 s^{-1} for the aged Ir/Ce850 sample (after long-term testing) presenting a mean Ir particle size of about 4.5 nm (values were not reported in Fig. 16B since the test was carried out at 600 °C, and we had to recalculate the conversion at 300 °C by assuming an activation energy of 58 kJ/mol). Such a non-linear structure sensitivity was recently reported by Fang et al. [52] for the bifunctional reaction of benzyl alcohol dehydrogenation over hydrotalcite-supported gold catalysts (*i.e.*, a noble metal supported on a basic material). This was explained by the similar drastic decrease in the concentration of CUS (corner and edge atoms as determined from particle modeling) as a function of the particle size for particles smaller than 4 nm, followed by a quasi-stable concentration of face sites for larger particle sizes. We propose a similar explanation in the present case, which might be related to the changes in linear/multi-bonded carbonyl species observed by DRIFT as a function of iridium dispersion (Fig. 8A). Ir particle modeling is consequently in progress in order to more quantitatively verify the changes in CUS concentration with particle size.

4.4.3. TOF calculated per interfacial site

For this TOF (Fig. 16C), the same trend as for the TOF calculated per surface Ir atom is observed, by considering either the Ir particle size or the ceria grain size. This result strongly confirms the key role of these interfacial sites in controlling the steps involving the cracking of the C_2 adspecies into C_1 adspecies. Here, a likely mechanism would involve the interfacial ceria site where the C_2 species are blocked and tilted against the Ir particle, allowing the CUS Ir atoms to preferentially attack the C–C bond and crack it into species migrating over the Ir particles. The methyl group from the acetate would then be cracked into carbon, which would be further oxidized into adsorbed CO and into hydrogen adspecies leading to the final syngas generation. It is also noted that these interfacial sites are likely to control the spillover of oxygen from the Ir particles (where the dissociation occurs easily) toward the ceria surface, thereby reoxidizing the ceria sites. For the case of Ni–Rh supported over nanocrystalline ceria particles [15], Kugai et al. also suggested that both the geometry (ceria particle size) and the electronic effects (metal-support interaction) controlled the crucial steps of C–C breaking at the ceria-Rh interface. The requirement for a tilted oxometallate adspecies for C–C bond breaking, as suggested in [53] but considering an ethoxy species instead of an acetate intermediate as in this work, also supports this key role of interfacial sites for the reforming process.

When both the ceria surface and metal dispersion are strongly decreased after deep sintering of Ir particles and ceria grains (as in the Ir/Ce850 sample), the concentration of interfacial sites linked to iridium CUS tends to diminish, and the key steps of the ethanol OSR process are inhibited. In this case, the alternative but much less active routes of ethanol activation occurring only on the ceria surface are favored, as revealed by a much higher selectivity toward acetaldehyde and ethylene as coke precursor.

The above discussion indicates that the overall rate-limiting steps of ethanol OSR are related both to surface diffusion of acetate adspecies and to their activation at the interfacial sites. Other steps dealing with initial ethanol adsorption and final syngas desorption are, in turn, considered not to control the overall rate.

4.5. Relationship between surface structure and catalyst stability

Upon the 60 h onstream aging test carried out at 650 °C, the Ir/Ce400 and Ir/Ce550 catalysts exhibited stable performance, while the Ir/Ce700 and Ir/Ce850 catalysts showed significant deactivation. Deactivation is usually related to carbon formation and/or to sintering of the metal particles, and strongly depends on the nature of the support and on the reaction conditions [54–56].

As reported in Tables 1 and 4, both Ir and ceria sintering were observed in similar ranges during these long-term aging tests for all the catalysts, though not to the same extent. These changes in Ir and ceria particle size upon aging are illustrated in Fig. 17, with each bar indicating the initial and final Ir and ceria particle sizes.

For Ir/Ce400 and Ir/Ce550, only moderate sintering of Ir particles and ceria is observed, and the two catalysts are found to be quite stable over the entire test period, with maintenance of full conversion of ethanol and high selectivity to syngas. For these two catalysts, we can conclude, in line with the previous analysis of the TOF values, that (i) a strong surface basicity linked to a high concentration of surface defects typical of large surface areas allows efficient water/oxygen activation and diffusion of adspecies toward the metal particles and (ii) a high concentration of CUS Ir sites close to ceria interfacial sites ensures the cracking of C_2 adspecies and their transfer into C_1 species according to an effective bifunctional process. These fast and permanent fluxes between the two active phases inhibit carbon accumulation on both the ceria surface and the metal particles, thus limiting deactivation.

In contrast, for the more sintered Ir/Ce700 and Ir/Ce850 catalysts, the surface migration of the adspecies along the ceria surface and their sequential oxidation are less effective. This favors the formation of side products on the less basic ceria surface such as (i) acetaldehyde formation via acetyl moieties, which does not require any further oxidation of the ethoxy species and (ii) the dehydration of ethoxy species into ethylene, leading to coke formation, as revealed by the TPO curves in Fig. 14A and to the encapsulating and filamentous coke observed on the aged Ir/Ce700 and Ir/Ce850 catalysts (Fig. 13). The considerable sintering also observed on the Ir particles, especially for the Ir/Ce850 catalyst, might also favor the buildup of polymeric carbon, due to much less efficient oxygen spillover between the ceria surface and the Ir particles. This kind of carbon deposit on or close to the metallic particles can

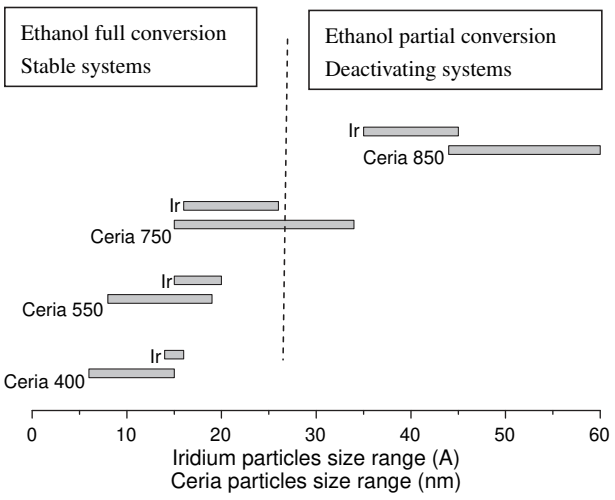

Fig. 17. Changes in Ir and ceria particle sizes upon long-term aging tests carried out at 650 °C for 60 h (initial to final values for each bar: from left- to right-hand side).

correspond to the TPO peaks at medium and high temperature, also shown in Fig. 14A.

From the above analysis, three cases can tentatively be distinguished in Fig. 17:

(i) For the highly dispersed catalysts (Ir/Ce400 and Ir/Ce550), moderate ceria sintering occurs upon long-term testing. The ceria dispersion is nevertheless maintained in a domain ensuring full conversion of ethanol and high stability. A significant SMSI effect arising from the high concentration of ceria defects tends to limit the Ir sintering in this case, keeping the bifunctional mechanism effective throughout the test.

(ii) For the less-dispersed Ir/Ce700 catalyst, complete ethanol conversion occurs at the beginning of the test, but as soon as ceria sinters beyond a size limit of 25–30 nm, the conversion decreases and a progressive deactivation occurs, due to the formation of coke on the ceria surface. This coking is itself a consequence of a lowered surface mobility of the oxygenate adspecies (less basic defect sites) that reinforces their likelihood of being dehydroxylated into coke precursors (ethylene). In this case, the Ir dispersion also suffers from sintering due to decreased interaction between the sintered ceria surface and the Ir particles.

(iii) For the initially poorly dispersed catalyst (Ir/Ce850), the lack of surface defects (resulting in very weak basicity) prevents any surface transfer and partial oxidation of the ethoxy toward the Ir particles. As a consequence, slow side reactions such as acetaldehyde and ethylene formation are favored, making the system more monofunctional than bifunctional. Only partial conversion of ethanol is observed from the beginning of the test, and continuous deactivation occurs throughout the entire testing period, due to the progressive poisoning of metal and support caused by carbon deposits. The coking of Ir particles is also a reason for C–C breaking inhibition. The still more extended Ir sintering observed in this case confirms the key role of the interaction between the ceria surface and the metal phase.

5. Conclusions

A systematic study for identifying the key relationships between the catalyst morphology/structure and catalytic performance in ethanol oxidative steam reforming has been carried out over a series of Ir/CeO_2 catalysts. The dispersion of both the ceria support and the noble metal phase is shown to strictly control key parameters such as the diffusion of oxygenated adspecies along the ceria surface, the surface basicity, and the concentration of coupled sites formed at the metal/support interface between peripheral ceria defects and CUS on Ir particles. All of these factors are found to be critical for ethanol conversion, selectivity toward hydrogen production, and resistance to aging upon long-term testing. From these statements, from ceria surface diffusion modeling and from the calculation of three types of TOF according to the active sites considered, it was demonstrated that ethanol OSR on noble metal/ceria catalysts is a structure sensitive reaction, leading to either an effective bifunctional or a more monofunctional mechanism depending on the domains of ceria and iridium dispersion. Well-dispersed active phases therefore lead to stable and selective catalysts following a bifunctional reforming mechanism, while poorly dispersed phases lead to unstable and unselective catalysts, proceeding essentially along a monofunctional mechanism. Such an original and quantified structure sensitivity analysis should provide strong guidelines for further catalyst and process developments.

Acknowledgments

Financial support from the National Natural Science Foundation of China (Grant No. 20773119) and the French Embassy in China is greatly appreciated.

References

[1] Ramirez de la Piscina, N. Homs, Chem. Soc. Rev. 37 (2008) 2459–2467.
[2] V. Fierro, O. Akdim, H. Provendier, C. Mirodatos, J. Power Sour. 145 (2005) 659–666.
[3] F. Frusteri, S. Freni, V. Chiodo, S. Donato, G. Bonura, S. Cavallaro, Int. J. Hydrogen Energy 31 (2006) 2193–2199.
[4] E. Vesselli, G. Comelli, R. Rosei, S. Frusteri, S. Cavallaro, Appl. Catal. A 281 (2005) 139–147.
[5] G. Jacobs, R.A. Keogh, B.H. Davis, J. Catal. 245 (2007) 326–337.
[6] V. Fierro, O. Akdim, C. Mirodatos, Green Chem. 5 (2003) 20–24.
[7] V. Fierro, V. Klouz, O. Akdim, C. Mirodatos, Catal. Today 75 (2002) 141–144.
[8] R.W. van den Brink, M. Krzan, M.M.R. Feijen-Jeurissen, R. Louw, P. Mulder, Appl. Catal. B 24 (2000) 255–264.
[9] P.E. Marti, M. Maciejewski, A. Baiker, Appl. Catal. B 4 (1994) 225–235.
[10] T. Miki, T. Ogawa, M. Haneda, N. Kakuta, A. Ueno, S. Tateishi, S. Matsuura, M. Sato, J. Phys. Chem. 94 (1990) 339–345.
[11] F. Auprêtre, C. Descorme, D. Duprez, Catal. Commun. 3 (2002) 263–267.
[12] L. Fan, K. Fujimoto, J. Catal. 172 (1997) 238–242.
[13] M.M. Pakulska, C.M. Grgicak, J.B. Giorgi, Appl. Catal. A 332 (2007) 124–129.
[14] J. Kugai, S. Velu, C. Song, Catal. Lett. 101 (2005) 255–264.
[15] J. Kugai, V. Subramani, C. Song, M.H. Engelhard, Y.-H. Chin, J. Catal. 238 (2006) 430–440.
[16] W. Cai, B. Zhang, Y. Li, Y. Xu, W. Shen, Catal. Commun. 8 (2007) 1588–1594.
[17] W. Cai, F. Wang, E. Zhan, A.C. Van Veen, C. Mirodatos, W. Shen, J. Catal. 257 (2008) 96–107.
[18] A. Birot, F. Epron, C. Descorme, D. Duprez, Appl. Catal. B 79 (2008) 17–25.
[19] S. Bernal, J.J. Calvino, G.A. Cifredo, A. Laachir, V. Perrichon, J.M. Herrmann, Langmuir 10 (1994) 717–721.
[20] C. Mirodatos, Catal. Today 9 (1991) 83–95.
[21] C. Descorme, D. Duprez, Appl. Catal. A 202 (2000) 231–241.
[22] F. Dong, A. Suda, T. Tanabe, Y. Nagai, H. Sobukawa, H. Shinjoh, M. Sugiera, C. Descorme, D. Duprez, Catal. Today 90 (2004) 223–229.
[23] U.S. Ozkan, Y. Cai, M.W. Kumthekar, J. Catal. 149 (1994) 375–389.
[24] H. Song, U.S. Ozkan, J. Catal. 261 (2009) 66–74.
[25] K. Tomishige, Y. Ikeda, T. Sakaihori, K. Fujimoto, J. Catal. 192 (2000) 355–362.
[26] Z.Y. Ma, C. Yang, W. Wei, W.H. Li, Y.H. Sun, J. Mol. Catal. A 227 (2005) 119–124.
[27] W. Khaodee, B. Jongsojit, S. Assabumrungrat, P. Praserthdam, S. Goto, Catal. Commun. 8 (2007) 548–556.
[28] S. Scrie, C. Crisafulli, R. Maggiore, S. Minico, S. Galvagno, Appl. Sur. Sci. 136 (1998) 311–320.
[29] J.C. Lavalley, Catal. Today 27 (1996) 377–401.
[30] S. Sato, R. Takahashi, M. Kobune, H. Gotoh, Appl. Catal. A 356 (2009) 57–63.
[31] C. de Leitenburg, A. Trovarelli, J. Kaspar, J. Catal. 166 (1997) 98–107.
[32] L.O.O. Costa, A.M. Silva, L.E.P. Borges, L.V. Mattos, F.B. Noronha, Catal. Today 138 (2008) 147–151.
[33] L. Xue, C. Zhang, H. He, Y. Teraoka, Appl. Catal. B 75 (2007) 167–174.
[34] P. Zimmer, A. Tschope, R. Birringer, J. Catal. 205 (2002) 339–345.
[35] P. Ratnasamy, D. Srinivas, C.V.V. Satyanarayana, P. Manikandan, R.S. Senthil Kumaran, M. Sachin, V.N. Shetti, J. Catal. 221 (2004) 455–465.
[36] F. Giordano, A. Trovarelli, C. Leienburg, M. Giona, J. Catal. 193 (2000) 273–282.
[37] A. Erdohelyi, J. Rasko, T. Kecskes, M. Toth, M. Domok, K. Baan, Catal. Today 116 (2006) 367–376.
[38] A. Yee, S.J. Morrisson, H. Idriss, J. Catal. 191 (2000) 30–45.
[39] L.V. Mattos, J. Catal. 233 (2005) 453–463.
[40] A.M. Da Silva, K.R. De Souza, G. Jacobs, U. Graham, B.H. Davis, L.V. Mattos, F.B. Norohna, Appl. Catal. B: Environ. 102 (2011) 94–109.
[41] F.R. Sarria, J.C. Vargas, A.C. Roger, A. Kiennemann, Catal. Today 133–135 (2008) 149–153.
[42] A.E. Galetti, M.F. Gomez, L.A. Arrua, M.C. Abello, Appl. Catal. A 348 (2008) 94–102.
[43] N. Laosiripojana, S. Assabumrungrat, Appl. Catal. B 66 (2006) 29–39.
[44] S.M. Gates, J.N. Russel Jr., J.T. Yates Jr., Surf. Sci. 171 (1986) 111–134.
[45] A.F. Lee, D.E. Gawthrope, N.J. Hart, K. Wilson, Surf. Sci. 548 (2004) 200–208.
[46] M. Benkhaled, C. Descorme, D. Duprez, S. Morin, C. Thomazeau, D. Uzio, Appl. Catal. A 346 (2008) 36–43.
[47] A. Trovarelli, Catal. Rev. Sci. Eng. 38 (1996) 439–443.
[48] R.A. van Santen, Acc. Chem. Res. 42 (2009) 57–66.
[49] E. Mamontov, T. Egami, R. Brezny, M. Koranne, S. Tyagi, J. Phys. Chem. B 104 (2000) 11110–11116.
[50] G.B. Sun, K. Hidajat, X.S. Wu, S. Kawi, Appl. Catal. B: Environ. 81 (2008) 303–312.
[51] Y. Madier, C. Descorme, A.M. Le Govic, D. Duprez, J. Phys. Chem. B 103 (50) (1999) 10999–11006.
[52] W. Fang, J. Chen, Q. Zhang, W. Deng, Y. Wang, Chem. Eur. J. 17 (2011) 1247–1256.
[53] P.-Y. Sheng, A. Yee, G.A. Bowmaker, H. Idriss, J. Catal. 208 (2002) 393.
[54] A.N. Fatsikostas, X.E. Verykios, J. Catal. 225 (2004) 439–452.
[55] M.A. Goula, S.K. Kontou, P.E. Tsiakaras, Appl. Catal. B 49 (2004) 135–144.
[56] A.N. Fatsikostas, D.I. Kondarides, X.E. Verykios, Catal. Today 75 (2002) 145–155.